Journal of Energy Storage 183 (2027) 125582

Contents lists available at ScienceDirect

Journal of Energy Storage

journal homepage: www.elsevier.com/locate/est

Research papers

A systematic sensitivity study of electrolyte transport parameters in physico-chemical battery models

Maximilian Gruber [a,b,1,*], Jonas Günther [a,c,1], Frank Hofmann [a], Daniel Rutz [a], Dominik Wycisk [a], Nils Stumböck [a], Marc Oldenburger [a], Ernst Richter [a], Ralf Moos [c], Jan Philipp Schmidt [c], André Weber [b]

[a] Mercedes-Benz AG, Mercedesstraße 120, Stuttgart, 70372, Baden-Württemberg, Germany
[b] Karlsruhe Institute of Technology (KIT), Institute for Applied Materials (IAM-ET), Adenauerring 20b, Karlsruhe, 76131, Baden-Württemberg, Germany
[c] University of Bayreuth, Bavarian Center for Battery Technology (BayBatt), Universitätsstraße 30, Bayreuth, 95447, Bavaria, Germany

ARTICLE INFO

Keywords:
Lithium-ion battery
Physico-chemical modelling
Doyle–Fuller–Newman model (DFN)
Electrolyte
Sensitivity analysis

ABSTRACT

Physico-chemical Doyle–Fuller–Newman (DFN/P2D) battery models rely on four electrolyte transport functions that depend on concentration and temperature: ionic conductivity σ, apparent diffusion coefficient D_{app}, cation transference number t_+^0, and thermodynamic factor χ. Published parameterisations of these functions vary widely, yet existing sensitivity studies typically apply uniform perturbations, obscuring the distinct roles of parameter magnitude and concentration dependence. Here, we introduce a dual variation strategy that systematically separates these effects via physically motivated, one-at-a-time perturbations referenced to a common concentration. Using a P2D model across two cell designs, two operating scenarios (fast-charging and discharge), and three temperatures (5, 25, 45 °C), we assess the impact on fast-charging time and discharge capacity. Within the literature-informed variation space of this study, model predictions are more sensitive to the concentration dependence than to uniform magnitude shifts for most transport parameters. The sensitivities depend strongly on operating scenario and temperature. In particular, accurate representation of the apparent diffusion coefficient, thermodynamic factor, and transference number at relevant concentration ranges is critical. Sensitivities increase markedly towards 5 °C but the sensitivity ranking remains consistent across cell designs. Single-concentration parameterisations are insufficient; the concentration dependence must be experimentally resolved to enable reliable DFN-based predictions.

1. Introduction

Physico-chemical battery models based on the Doyle–Fuller–Newman (DFN) framework [1,2] have become established tools for the design and analysis of lithium-ion batteries [3,4]. Their predictive capability critically depends on accurate parameterisation, which is required not only to reproduce cell voltage behaviour but also to resolve the individual physically meaningful overpotential contributions and their interactions. This is essential for reliably predicting the impact of design modifications. Among the various model parameters, the four electrolyte transport functions, each depending on salt concentration c and temperature T, are particularly crucial in this context:

1. the ionic conductivity $\sigma(c,T)$ in $\mathrm{S\,m^{-1}}$,
2. the apparent (salt) diffusion coefficient $D_{app}(c,T)$ in $\mathrm{m^2\,s^{-1}}$,
3. the cation transference number $t_+^0(c,T)$ in 1, defined in the solvent-fixed reference frame [5], and
4. the thermodynamic factor $\chi(c,T) = 1 + \partial \ln f_\pm / \partial \ln c$ in 1, following the PyBaMM (Python Battery Mathematical Modelling) convention [6], where $f_\pm$ denotes the mean ionic activity of the electrolyte.

These four functions enter two governing equations for electrolyte transport derived from concentrated solution theory [1,5]. The material balance on the lithium salt in the electrolyte phase reads

$$\varepsilon_e \frac{\partial c_e}{\partial t} = \nabla \cdot \left(D_{eff} \left(1 + \frac{d \ln c_0}{d \ln c_e} \right) \nabla c_e \right) + \frac{1 - t_+^0}{z_+ \nu_+ F} a_s j_n , \tag{1}$$

where D_{eff} is the effective salt diffusion coefficient, c_0 the solvent concentration, z_+ and ν_+ the cation charge number and stoichiometric

* Corresponding author at: Karlsruhe Institute of Technology (KIT), Institute for Applied Materials (IAM-ET), Adenauerring 20b, Karlsruhe, 76131, Baden-Württemberg, Germany.
E-mail address: maximilian.m.gruber@mercedes-benz.com (M. Gruber).
[1] These authors contributed equally to this work.

https://doi.org/10.1016/j.est.2026.125582
Received 7 July 2026; Received in revised form 6 October 2026; Accepted 4 November 2026
Available online 16 November 2026
2352-152X/© 2026 The Authors. Published by Elsevier Ltd. This is an open access article under the CC BY license (http://creativecommons.org/licenses/by/4.0/).
Open access funding enabled and organized by Projekt DEAL.

coefficient, ε_e the electrolyte volume fraction, a_s the specific interfacial area, and j_n the local pore-wall flux [1]. The ionic current density in the electrolyte obeys [1]

$$\mathbf{i}_e = -\kappa_{eff}\,\nabla\Phi_e + \frac{\nu\,\kappa_{eff}\,RT}{\nu_+\,z_+\,F}\,(1-t_+^0)\left(1+\frac{d\ln f_\pm}{d\ln c_e}\right)\nabla\ln c_e\,, \tag{2}$$

where κ_{eff} is the effective ionic conductivity, $\nu=\nu_+ + \nu_-$ the total number of ions per formula unit, and $f_\pm$ the mean molar activity coefficient. For $LiPF_6$ — a binary 1:1 salt ($z_+=\nu_+=1$, $\nu=2$) in a liquid solvent — three simplifications apply: the solvent concentration is approximately constant ($d\ln c_0/d\ln c_e \approx 0$), the stoichiometric prefactors reduce to unity and 2 respectively, and the activity-coefficient derivative is absorbed into the thermodynamic factor $\chi = 1+\partial\ln f_\pm/\partial\ln c$. Denoting $\sigma\equiv\kappa$ and $D_{app}\equiv D$, Eqs. (1)–(2) simplify to

$$\varepsilon_e\frac{\partial c_e}{\partial t} = \nabla\cdot\left(D_{app,eff}\,\nabla c_e\right) + \frac{1-t_+^0}{F}\,a_s\,j_n\,, \tag{3}$$

$$\mathbf{i}_e = -\sigma_{eff}\,\nabla\Phi_e + \frac{2\,\sigma_{eff}\,RT}{F}\,(1-t_+^0)\,\chi\,\nabla\ln c_e\,. \tag{4}$$

Eq. (4) shows that σ determines the ohmic potential drop in the electrolyte phase (first term), while the product $(1-t_+^0)\,\chi$ scales the concentration overpotential (second term). In Eq. (3), D_{app} governs the rate at which concentration gradients relax, and t_+^0 controls which fraction of the ionic current produces concentration gradients via the factor $(1-t_+^0)$. Together, these four functions control the concentration overpotential, ohmic losses in the electrolyte phase, and the limiting current density. At high C-rates, they also determine the onset of lithium plating [7,8]. At low temperatures, sluggish transport amplifies these effects, making accurate parameterisation essential [9]. Beyond physics-based cell design, impedance spectroscopy and relaxation voltage are increasingly exploited for battery characterisation and state-of-health estimation [10–12].

Published parameter sets for $LiPF_6$ in carbonate solvents disagree substantially, particularly for D_{app} and t_+^0 (Table 1). Despite this uncertainty, many modelling studies adopt a single parameter set without testing their sensitivity to that choice [13–15].

The complexity of the P2D framework makes systematic sensitivity studies challenging. Existing analyses perturb each transport function by a fixed percentage [16,17]. This uniform scaling conflates the absolute value of a transport function (*magnitude*) with its concentration dependence (*shape*). Existing studies have not systematically varied individual electrolyte transport functions and quantified their separate effects on model accuracy.

We introduce a dual variation strategy that decouples magnitude and shape:

- **Magnitude variations and constant profiles**: global scaling (±20%) keeps the concentration dependence. Constant (flat) profiles remove it, as frequently adopted when concentration -dependent data are unavailable [1,2].
- **Shape variations**: physically motivated modifications of individual curve features (e.g. decay type, sigmoid slope, bathtub depth), all anchored at $c_{anchor} = 1.2\,mol\,L^{-1}$, the typical initial electrolyte concentration in commercial cells.

We apply these variations one at a time (OAT) to a P2D model of the cylindrical LG M50T 21700 cell, parameterised after Chen et al. [14], O'Regan et al. [18], O'Kane et al. [19], and Li et al. [20]. Two cell designs (denoted as Energy and Power Cell), two operational scenarios (fast-charging and continuous discharge), and three temperatures are simulated. Sensitivity is quantified by changes in isothermal fast-charging time from 10% to 80% state of charge (SoC) and delivered capacity at 1 C discharging.

The goal is to identify which transport functions and concentration ranges require the highest measurement precision. This provides experimentalists with a clear prioritisation for resource allocation.

2. Literature analysis

This section reviews published electrolyte transport data for $LiPF_6$ in carbonate solvents and the limitations of existing sensitivity analyses.

2.1. Published electrolyte transport data

Table 1 compiles reported values of the four electrolyte transport functions at $c = 1.0\,mol\,L^{-1}$ and $T = 25\,°C$ for $LiPF_6$ in carbonate solvents. Across all solvent systems (EC:DMC, EC:EMC, EC:DEC, EMC), the literature contains more than 20 independent sources. However, the number of data sets per parameter is small and unevenly distributed. For the apparent diffusion coefficient D_{app}, no single solvent system is covered by more than one publication. Modellers are therefore frequently forced to combine parameter sets from different publications, often without matching the solvent composition. Table 1 quantifies the inter-study reproducibility within the best-covered same-solvent system for each property. The resulting picture reveals that only ionic conductivity is well-characterised; the remaining three properties carry substantial uncertainty even when the solvent system is held constant. The coefficient of variation (CV = standard deviation divided by the mean, expressed as a percentage) quantifies the relative scatter among independent measurements within the same solvent system. A CV below 6% indicates good reproducibility, whereas values above 20% signal that independent sources diverge beyond typical measurement uncertainty.

The spread in Table 1 underscores the uneven state of electrolyte characterisation. For σ and t_+^0, the table refers specifically to same-solvent comparisons. For χ, the two EC:EMC values differ by a sign change, which is not a measurement-noise effect but a consequence of the different t_+^0 values used in the derivation of χ from concentration-cell data. The cross-solvent scatter, which is the range a modeller actually encounters in the literature, is even larger.

Ionic conductivity is the only well-characterised property. EIS is a well-standardised technique [26], and two independent EC:EMC sources agree within $\sigma = 8.9$–$9.6\,mS\,cm^{-1}$ (CV = 4%). EC:DMC data from six sources span 10.2–$11.9\,mS\,cm^{-1}$ (CV = 6%). The full cross-solvent range of 4.5–$11.9\,mS\,cm^{-1}$ is dominated by the difference between pure EMC [23] and EC-containing mixtures. Since DFN modellers routinely adopt parameter sets from different solvent systems, this cross-solvent scatter motivates the ±20% magnitude variations described below.

The apparent diffusion coefficient D_{app} is the most data-scarce property. Only two publications [21,23] report D_{app} at the reference point, each for a different solvent. A same-system reproducibility assessment is therefore impossible. Five additional publications report the chemical diffusion coefficient D_{chem}, with two EC:EMC sources resulting in 1.3×10^{-6} and $1.8\times10^{-6}\,cm^2\,s^{-1}$ [21,22] (CV = 23%). The conversion between D_{app} and D_{chem} requires the thermodynamic factor, which itself carries large uncertainty (see below). Beyond the scarcity of data, the determination of D_{app} from restricted-diffusion or polarisation experiments demands stable lithium reference electrodes and suppression of convective transport, which limits reproducibility across laboratories. Lehnert et al. [27,28] showed that side reactions at the lithium interface can further bias polarisation-based measurements. The steepness of the concentration dependence also varies between sources, motivating the shape variations described below.

The transference number t_+^0 shows the widest relative spread. Even within the same solvent system (EC:DEC) and using the same method (galvanostatic polarisation combined with concentration cells), two independent groups report $t_+^0 = 0.11$ [24] and 0.16 [25] (CV = 25%). Across all solvents and methods, eight measured values span 0.11–0.50 [22,23,26,29]. Four additional literature values are assumed rather than measured and are excluded from this count. The method is the dominant driver: galvanostatic-polarisation approaches report $t_+^0 < 0.2$, while Hittorf and NMR-based methods return $t_+^0 = 0.3$–0.5 [26,30]. Beyond this scatter, negative transference numbers have been reported

Table 1
Inter-study reproducibility of electrolyte transport parameters for $LiPF_6$ in carbonate solvents at $c = 1.0\,mol\,L^{-1}$, $T = 25\,°C$ given as minimum (Min), maximum (Max) values and the coefficient of variation (CV). For each property, the best-covered same-solvent system is evaluated. Where no multi-source same-solvent comparison exists, this is marked explicitly.

Property	Unit	System	Min	Max	CV	Sources
σ	$mS\,cm^{-1}$	EC:EMC	9.0	9.5	4%	[21,22]
D_{app}	$cm^2\,s^{-1}$	no same-solvent multi-source comparison available				[21,23]
t_+^0	–	EC:DEC	0.11	0.16	25%	[24,25]
χ	–	EC:EMC	−0.03	2.2	–	[21,22]

in polymer electrolytes [31] and predicted by molecular dynamics [32,33]. A negative transference number implies that the net lithium flux in the electrolyte reverses direction at high concentrations, fundamentally altering concentration gradient dynamics under high-rate operation.

The thermodynamic factor χ is derived indirectly from concentration-cell measurements combined with t_+^0 [21,34]. Its accuracy therefore propagates the uncertainty of the transference number. For EC:EMC, the two available sources report $\chi = -0.03$ [22] and $\chi = 2.2$ [21] at the reference point — a qualitative disagreement that reflects different underlying t_+^0 values. Across all solvents, six values from four publications span this same range (CV = 64%), making χ the most uncertain property. The shape-variation analysis below examines whether the bathtub depth and the high-concentration tail type affect cell-level predictions.

The Advanced Electrolyte Model (AEM) [35,36] predicts all four transport functions from a molecular solvation framework, validated against experimental data by Logan et al. [37]. AEM is widely used in industrial battery modelling as a source of electrolyte transport functions. In this study, AEM predictions are rescaled to match the baseline at c_{anchor} and included as plausible alternative shapes in the shape-variation analysis. After rescaling, the AEM curves represent physically motivated concentration profiles from a molecular solvation framework rather than independent references. The AEM has been validated against measured transport data for carbonate electrolytes [35,37]. A systematic comparison across additional electrolyte formulations is left to future work. No conclusion of this study relies on the absolute accuracy of the AEM. They provide an additional data point in the shape-variation space to test whether qualitatively different profiles lead to different cell-level predictions.

All transport data discussed above refer to binary salt-in-solvent electrolytes without additives. Commercial electrolytes contain 1–5 wt% additives that modify transport properties, particularly at interfaces, for instance, by forming the solid electrolyte interphase (SEI). The present analysis applies to bulk electrolyte transport functions as parameterised in P2D models, where additive effects are typically subsumed into interfacial kinetics rather than into the electrolyte transport functions.

2.2. Previous sensitivity studies

The studies reviewed below employ different electrolyte systems, cell chemistries, and operating conditions, which limits direct quantitative comparison but reveals consistent qualitative trends regarding the role of electrolyte transport.

Sensitivity analyses of DFN models have been performed with both global (Sobol indices, polynomial chaos) and local one-at-a-time (OAT) methods [16,17,38–40]. Across these studies, the role of electrolyte transport functions follows a consistent pattern.

Under moderate operating conditions, electrolyte parameters rank below electrode capacity and kinetic parameters. Zonta et al. [16] computed time-resolved Sobol indices for 24 DFN parameters during a drive cycle and found that σ, D_{app}, t_+^0, and χ contribute negligibly to the output variance. However, several studies demonstrate that this ranking is not universal. Hadigol et al. [38] showed that the sensitivity ranking shifts substantially between 0.25C and 4C discharge, with electrolyte parameters gaining importance at higher rates. Li et al. [39] confirmed this in an OAT analysis of 26 parameters: electrolyte transport ranked as moderately sensitive overall, but its importance increased at high currents. Chen et al. [17] quantified that operating conditions can shift individual parameter sensitivities by up to two orders of magnitude, with high C-rates and low temperatures amplifying the electrolyte contribution.

Ma et al. [40] extended the analysis to terminal voltage, anode overpotential, and delivered capacity at 5, 25, and 40 °C. They found that parameters sensitive to the anode potential differ from those sensitive to the terminal voltage. At low temperatures, electrolyte parameters dominate the anode-potential response. These findings directly motivate the design of the present study, which evaluates both delivered capacity and fast-charging time, directly linked to minimum anode overpotential, across three temperatures.

Taken together, these studies compare electrolyte transport with electrode kinetic and capacity parameters and show that their relative importance depends on C-rate and temperature, with electrolyte transport gaining weight at high rates and low temperatures [17,38–40]. A comprehensive global sensitivity analysis of all electrolyte and electrode parameters is therefore not repeated here. Instead, the present study complements these analyses by resolving the electrolyte transport functions in greater detail. All reviewed studies share one structural limitation: electrolyte transport functions are perturbed as scalars or scaled uniformly. No study has varied the concentration dependence independently from the absolute value. This conflation obscures whether the model responds to the overall level of a transport function or to specific features of its c-dependent profile. The present study addresses this gap.

3. Sensitivity study

3.1. Model and simulation setup

All simulations are carried out using a MATLAB/Simulink implementation of the pseudo-two-dimensional (DFN/P2D) model, fully aligned with the implementation in PyBaMM [6]. The baseline parameterisation of the cylindrical LG M50T 21700 cell (NMC811/graphite, nominal capacity 5.0 Ah) follows Chen et al. [14], with improved kinetic and transport parameters from O'Regan et al. [18]. The OCV and balancing data of both electrodes are updated from Li et al. [20], based on findings from O'Kane et al. [19]. The kinetic and transport activation energies are taken from additional literature sources to better match previous experiences, namely [13,41,42]. Baseline electrolyte transport properties are taken from Landesfeind [21], assuming a $LiPF_6$ electrolyte in EC:EMC (3:7 w:w). An overview of all parameters including source is provided in the Supporting Information, Table S1.

To improve the generalisability of the sensitivity analysis, two cell designs are considered:

- **Energy Cell** — original (thick) electrodes with 75.6 µm and 85.2 µm positive and negative electrode thickness, respectively. This results in an areal loading of approximately 4.87 $mAh\,cm^{-2}$, representative of energy-optimised cells, and a total capacity of 5 Ah.

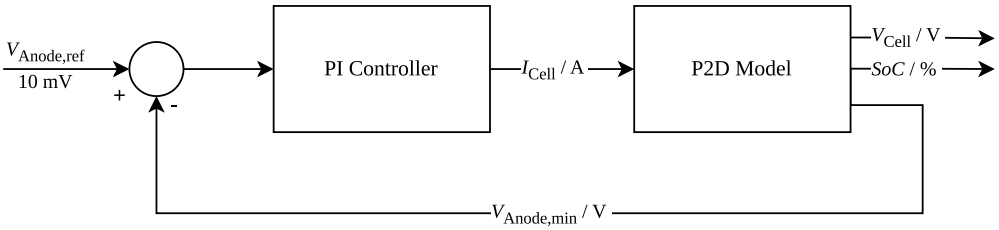


Fig. 1. Block diagram of model-based anode-potential-controlled fast-charging from 10% to 80% SoC with minimum anode potential being regulated to a setpoint of 10 mV.

- **Power Cell** — derived thin electrodes with a 38% reduction in coating thickness, assuming identical porosity and total electrode area, resulting in an areal loading of approximately 3 mAh cm^{-2} and a total capacity of 3.1 Ah. This represents a moderate-power configuration rather than a state-of-the-art extreme-fast-charging (XFC) design (typically 2.0–2.5 mAh cm^{-2}). Since the sensitivity ranking is preserved across both designs despite different electrode thicknesses, we expect the qualitative conclusions to hold for thinner electrodes as well.

Throughout this work, electrode labels follow the discharge convention: the negative electrode (graphite) is termed anode and the positive electrode (NMC811) is termed cathode. Simulations are performed at three temperatures: 5 °C, 25 °C, and 45 °C assuming isothermal conditions. All conclusions refer to this temperature range. The P2D model describes a representative cross-section of the electrode stack, resolving transport exclusively in the through-plane direction. In-plane inhomogeneities (tab placement effects, thermal gradients along the jelly roll) are not considered.

Two operational scenarios are studied:

- **Fast-charging** — anode-potential-controlled fast-charging from 10% to 80% SoC, where the minimum anode potential is regulated to a setpoint of 10 mV vs. Li/Li$^+$, as represented in Fig. 1. A current limit of 10 C is imposed, although it is rarely reached during the simulation study. An additional voltage controller limits the full cell voltage to operate at maximum 4.2 V.
- **Continuous discharge** — constant-current discharge at 1 C until the lower cutoff voltage of 2.8 V is reached. The 1 C rate was chosen as a standardised reference that produces moderate transport stress. While automotive drive cycles typically operate at variable rates below 1 C average, the constant-current protocol isolates the electrolyte transport response from current-profile effects and represents a conservative bound for sustained high-power demand as present e.g. in motor sport or power-tool applications.

3.2. Generation of electrolyte parameter variations

All four electrolyte transport functions are varied independently using a one-at-a-time (OAT) approach. The baseline transport functions are taken from Landesfeind [21]. Two complementary variation types are applied, as visualised in Figs. 2 and 3.

3.2.1. Magnitude variations and constant profiles

Two groups of variations are generated from the baseline curve. Magnitude variations (items 1 and 2) scale the curve by ±20% and keep its concentration dependence. Constant profiles (items 3 to 5) replace the curve by its value at c_{anchor}. A constant profile keeps the anchor value and removes the concentration dependence. It is therefore the limiting case of a shape variation. The constant profiles with a ±20% offset combine both effects. The variation types are:

1. **+20%**: global multiplication by 1.2.
2. **–20%**: global multiplication by 0.8.
3. **Flat**: a concentration-independent profile, where the baseline value at c_{anchor} is held constant across all concentrations.
4. **Flat + 20%**: flat profile scaled by +20%.
5. **Flat – 20%**: flat profile scaled by −20%.

The ±20% range reflects the typical inter-study spread observed in Table 1. For D_{app} and t_+^0 in particular, independent measurements diverge by at least this margin [21,26]. The flat variations additionally test whether the model is sensitive to the *concentration dependence itself*. Constant profiles are not applied to σ, because a concentration-independent conductivity destabilises the model (Section 4.3.1). This yields $3\times5+2 = 17$ variations plus one baseline, totalling 18 simulation inputs. We report the constant profiles together with the magnitude variations, because a single constant value is common modelling practice when concentration-dependent data are unavailable. The shape variations in Section 3.2.2, by contrast, preserve the anchor-point value and exclusively modify the functional form. The magnitude variations are illustrated in Fig. 2.

3.2.2. Shape variations

Shape variations modify the *concentration dependence* (i.e. the functional form) of each transport function while preserving its value at a common anchor concentration $c_{anchor} = 1.2\,\mathrm{mol\,L^{-1}}$. All shape variants pass through this point, thereby decoupling the effect of the curve profile from that of its absolute level. The choice of $c_{anchor} = 1.2\,\mathrm{mol\,L^{-1}}$ corresponds to the initial electrolyte concentration in the cell. Since all shape variants are pinned to the baseline at this concentration, the reported shape sensitivities specifically quantify the effect of deviations away from the operating point. A different anchor concentration would redistribute the attribution between magnitude and shape effects but would not change the total combined sensitivity.

For each parameter, we develop simple phenomenological models that reproduce the characteristic concentration profiles known from the literature while enabling systematic variation of individual curve features. Examples include the steepness of a rise, the type of a decay, or the sign of a slope. These models are not intended as physical theories. They serve as flexible generators of plausible concentration-dependent profiles for the sensitivity analysis. Each form is tied to a known physical feature, as explained for each function below. The same functional forms describe published data for other carbonate solvents and for $NaPF_6$ [21,24,29], and only the parameters change. The forms apply to liquid electrolytes with a conductivity maximum. They are not intended for polymer, solid or highly concentrated electrolytes. The model choices are deliberately simple (typically two to three tuneable features per parameter) to maintain a one-at-a-time variation strategy within the shape domain. Variations are computed at three reference temperatures (5 °C, 25 °C, and 45 °C). An overview of all shape variations is provided in Table 2 and illustrated in Fig. 3.

Ionic conductivity $\sigma(c,T)$. Simple polynomial fits, as commonly used in the literature [21,29], cannot reliably be extrapolated beyond their calibration range. We therefore model $\sigma(c)$ as a three-segment curve connected by smooth Hermite blending functions (ensuring C^1 continuity), with each segment capturing a distinct physical regime:

1. **Dilute regime** ($c < c_{trans}$, where c_{trans} denotes the transition concentration between the dilute and peak regimes, determined by the intersection of Eqs. (5) and (6)): a Kohlrausch-type rise [43],

$$\sigma_1(c) = \sigma_0 + A\,c\,(1 - K\sqrt{c}\,), \tag{5}$$

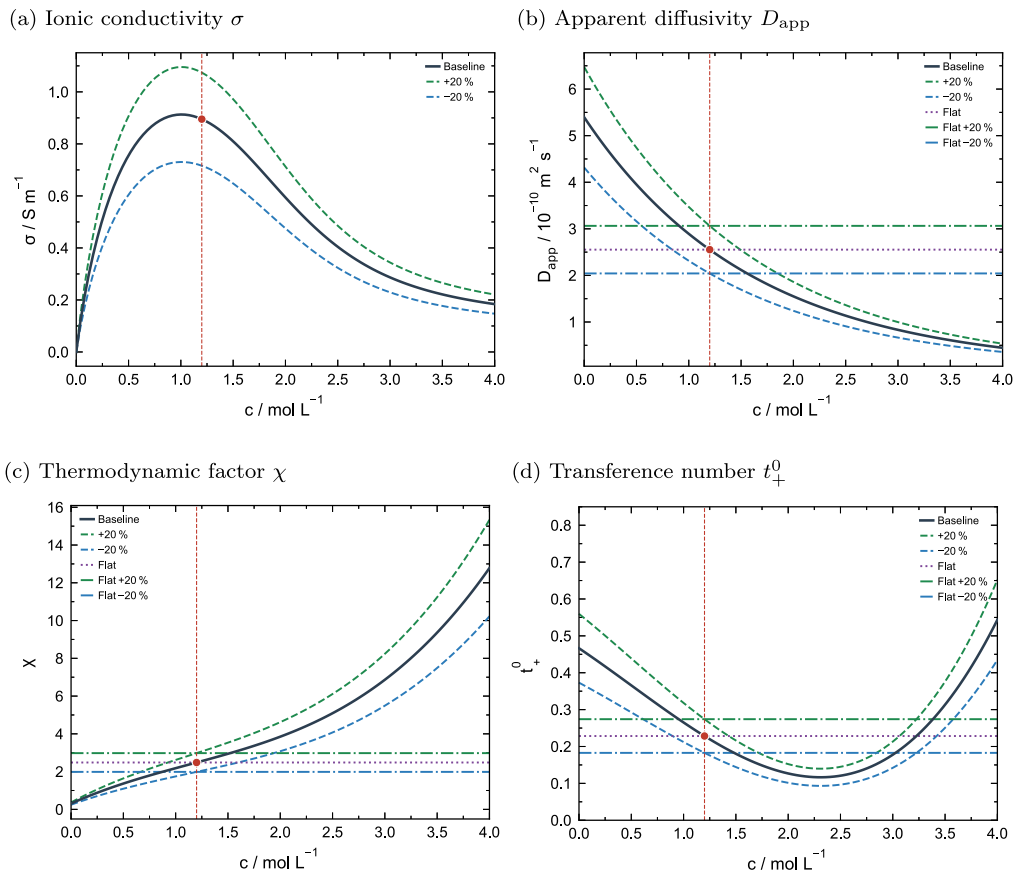


Fig. 2. Magnitude variations and constant profiles of the four electrolyte transport functions at 25 °C. (a) σ, (b) D_{app}, (c) χ, (d) t_+^0. Solid black: baseline (Landesfeind parameterisation). Dashed/dotted: ±20% scaling and flat (concentration-independent) profiles. Red marker: shared anchor point at $c_{anchor} = 1.2\,\mathrm{mol\,L^{-1}}$. (For interpretation of the references to colour in this figure legend, the reader is referred to the web version of this article.)

where σ_0 is a residual offset controlling the dilute-limit intercept. Even in nominally pure solvents, ionic impurities produce a small but measurable conductivity at $c \to 0$. Published data for different salt–solvent combinations show distinctly different dilute-limit intercepts [44]. The parameters A and K are analytically determined from continuity with the peak segment.

2. **Peak regime** ($c_{trans} \le c \le c_{decay}$, where $c_{decay} \approx 1.5\,\mathrm{mol\,L^{-1}}$ marks the onset of the high-concentration decay): a parabolic maximum,

$$\sigma_2(c) = \sigma_{max}\left[1 - \beta\,(c - c_{max})^2\right], \tag{6}$$

where σ_{max} and c_{max} are the peak conductivity and its location, and β controls the curvature. This segment captures the competition between increasing charge-carrier density and rising viscosity that produces the non-monotonic conductivity profile.

3. **Concentrated regime** ($c > c_{decay}$): one of three alternative decay functions that reflect competing mechanisms governing the conductivity decline at high concentration [7]: Gaussian (smooth bell-shaped suppression, as observed in moderately concentrated solutions [21]), single-exponential (dominated by ion-pair formation [37]), or viscosity-limited ($\sigma \propto c/\eta(c)$, following the Walden-rule picture [45]).

Two independent shape features are varied:

- The *rise offset* $\sigma_0/\sigma_{max} \in \{0\%, 5\%, 10\%\}$ modifies only the dilute-limit intercept and controls how steeply conductivity increases at low concentrations.
- The *decay type* $\in$ {Gaussian, exponential, viscosity} changes only the tail behaviour at high concentrations.

Both features are varied independently while preserving the peak position and the anchor-point value. This yields six σ-shape variations.

Apparent diffusion coefficient $D_{app}(c,T)$. We describe the concentration dependence of D_{app} by a single-exponential decay anchored at c_{anchor}:

$$D_{app}(c) = D_{anchor}\,\exp\left[-k\,(c - c_{anchor})\right], \tag{7}$$

where D_{anchor} is the baseline value at the anchor concentration and k is obtained from a log-linear fit to the baseline data. This functional form is motivated by the observation that D_{app} decreases approximately exponentially with concentration in most carbonate electrolytes [21,26], consistent with the viscosity-mediated Stokes–Einstein picture [5]. The exponential form guarantees $D_{app} > 0$ at all concentrations. This is a physical constraint that polynomial fits may violate when extrapolated [22]. The steepness parameter k is multiplied by factors of $\{0.25,\ 0.50,\ 1.50,\ 2.00\}$. These span the range from a nearly concentration-independent profile ($k \times 0.25$), as observed at elevated temperatures by Landesfeind [21], to a steeply declining one ($k \times 2.0$). The steep end is consistent with diffusion data reported by Nyman et al. [22] at lower temperatures. This generates four D_{app}-shape variations.

Transference number $t_+^0(c,T)$. Published data show that t_+^0 decreases monotonically with concentration, but the magnitude of the decline and whether t_+^0 remains positive at high salt content are debated. A sigmoidal function is chosen because it naturally describes a monotonic transition between two asymptotic values, with each of its four parameters controlling one physically distinct feature. This enables systematic investigation of whether the high-concentration asymptote, the transition location, or the decline steepness drives the cell-level sensitivity, while guaranteeing smooth, bounded profiles without oscillations or divergence:

$$t_+^0(c) = t_{high} - \frac{t_{high} - t_{low}}{1 + \exp\left[-(c - c_{mid})/w\right]}, \tag{8}$$

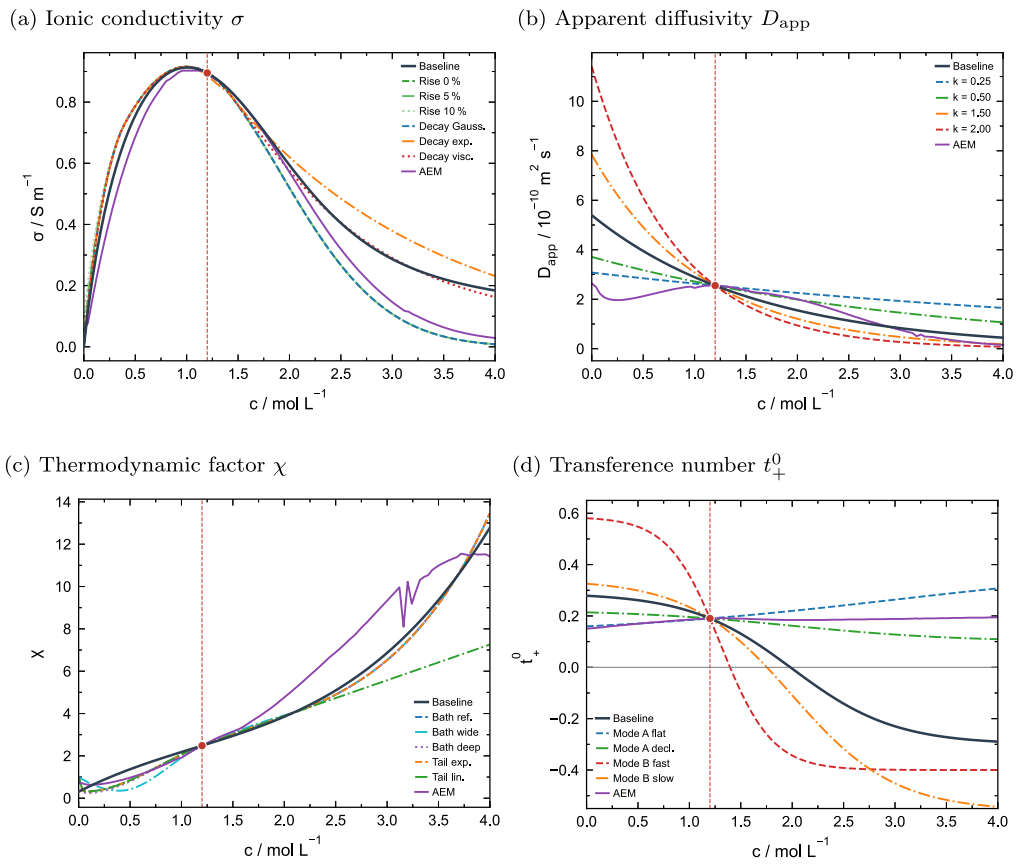


Fig. 3. Shape variations of the four electrolyte transport functions at 25 °C. (a) σ, (b) D_{app}, (c) χ, (d) t_+^0. Solid black: baseline (Landesfeind parameterisation). Coloured curves: shape variations preserving the anchor-point value (see Table 2 for variation definitions). Red marker: shared anchor point at $c_{\text{anchor}} = 1.2\,\text{mol L}^{-1}$ through which all variants pass. (For interpretation of the references to colour in this figure legend, the reader is referred to the web version of this article.)

where t_{high} is calibrated from the anchor value, and t_{low}, c_{mid}, w control the asymptotic high-concentration value, the inflection point, and the steepness of the transition, respectively. Two qualitatively distinct regimes are explored, reflecting the current debate in the literature on the sign of t_+^0 at elevated concentrations:

- **Mode A** ($t_{\text{low}} > 0$): t_+^0 remains positive across all concentrations, as assumed in most classical DFN parameter sets [21,29]. A *flat* profile ($t_{\text{low}} = 0.40$, broad sigmoid) and a moderately *declining* profile ($t_{\text{low}} = 0.10$) are considered.
- **Mode B** ($t_{\text{low}} < 0$): t_+^0 crosses zero at high concentrations, as observed in polymer electrolytes [31] and predicted by molecular dynamics (MD) simulations for systems with strong ion–ion correlations [32,33]. This scenario implies that in concentrated regions the net lithium flux reverses sign, fundamentally changing the concentration gradient dynamics. A *fast* zero-crossing (steep sigmoid near c_{anchor}, $c_{\text{mid}} = 1.3\,\text{mol L}^{-1}$) and a *slow* zero-crossing (broad sigmoid, $c_{\text{mid}} = 2.0\,\text{mol L}^{-1}$) are generated.

This yields four t_+^0-shape variations.

Thermodynamic factor $\chi(c,T)$. We construct the TDF from two piecewise-connected regions, matching the characteristic bathtub-plus-upturn profile reported across most carbonate electrolytes [21,29,46]:

- A *bathtub region* ($c \le c_{\text{anchor}}$), modelled by a piecewise cubic Hermite interpolant (PCHIP) through four control points. The boundary value $\chi(0) = 1$ is imposed by the Debye–Hückel limiting law [5].
- A *tail region* ($c > c_{\text{anchor}}$), modelled as either a linear or an exponential rise:

$$\chi_{\text{tail}}(c) = \begin{cases} \chi_0 + m_0\,(c - c_0), & \text{linear,} \\ \chi_0 + \dfrac{m_0}{\gamma}\left(e^{\gamma(c-c_0)} - 1\right), & \text{exponential,} \end{cases} \tag{9}$$

where χ_0 and m_0 denote the value and slope at the split point $c_0 = c_{\text{anchor}}$, and γ controls the curvature of the exponential tail. Some data sets show a strong upturn at high concentrations [29], associated with ion crowding and solvent depletion [46]. The linear tail variant tests whether this upturn is essential for accurate model predictions or whether a conservative linear extrapolation suffices. Three bathtub variants (reference, wide minimum, deep minimum) are each combined with the reference tail. Two tail variants (exponential, linear) are each combined with the reference bathtub. This yields five χ-shape variations via a one-at-a-time scheme within the model sub-components.

Summary and total variation count. Table 2 summarises all shape variations. In total, $6 + 4 + 4 + 5 = 19$ independent shape variations are generated. Only one parameter is varied per simulation while the other three remain at baseline. Additionally, Advanced Electrolyte Model (AEM) [35,36] predictions, scaled to match the baseline at c_{anchor}, are included as plausible alternative shapes for each parameter. Together with model-reference curves for σ and D_{app} and one shared baseline, this yields 26 shape-variation simulation inputs.

4. Results and discussion

4.1. Baseline performance

Fig. 4 shows the baseline fast-charging time and discharge capacity for both cell designs at three isothermal temperatures, obtained with

Table 2
Summary of shape variations for each electrolyte transport parameter. All variations share the anchor point at $c_{anchor} = 1.2\,mol\,L^{-1}$. The 'Segment' column indicates which part of the concentration dependence is modified.

Parameter	Variation title	Segment	Physical feature varied
σ	`rise_0/5/10pct`	dilute	Kohlrausch offset $\sigma_0 = 0$–10% of σ_{max}
	`decay_gauss/exp/visc`	concentrated	High-c decay: Gaussian, exponential, or viscosity-limited
D_{app}	`k_025/050/150/200`	full range	Exponential steepness factor $k\times\{0.25, 0.50, 1.50, 2.00\}$
t_+^0	`ModeA_flat`	full range	Positive, nearly constant ($t_{low} = 0.40$)
	`ModeA_decline`	full range	Positive, moderate decline ($t_{low} = 0.10$)
	`ModeB_fast`	$c > c_{anchor}$	Fast zero-crossing ($c_{mid} = 1.3\,mol\,L^{-1}$)
	`ModeB_slow`	$c > c_{anchor}$	Slow zero-crossing ($c_{mid} = 2.0\,mol\,L^{-1}$)
χ	`Bath_ref/wide/deep`	$c \le c_{anchor}$	Bathtub minimum: position, width, and depth
	`Tail_exp/linear`	$c > c_{anchor}$	High-c tail: exponential vs. linear rise

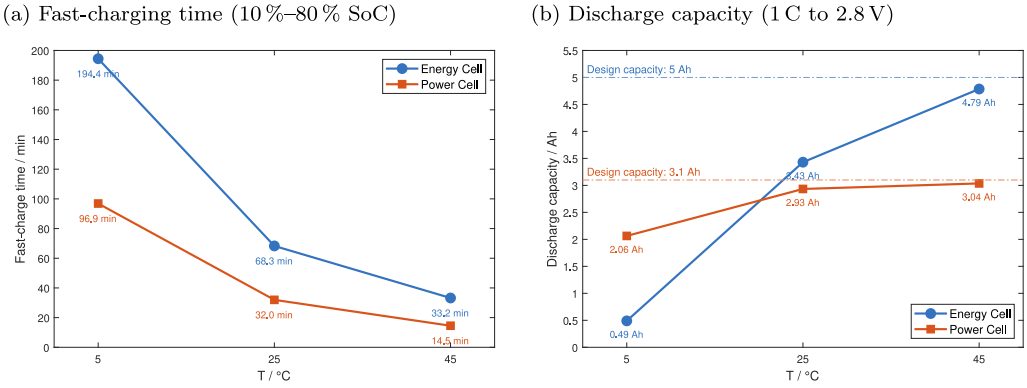


Fig. 4. Isothermal baseline performance of Energy Cell (dark bars) and Power Cell (light bars) at 5, 25, and 45 °C. (a) Fast-charging time from 10% to 80% SoC under anode-potential control (10 mV limit). (b) Delivered capacity during 1 C constant-current discharge to 2.8 V cutoff. All simulations use the unperturbed Landesfeind parameterisation.

the unperturbed Landesfeind electrolyte parameterisation [21]. The detailed simulation profiles including full cell and electrode voltages, and the maximum electrolyte concentration gradient are provided in the Supporting Information, Figures S2–S5. In case of the charging profiles, these include the charging current and minimum anode potential to show the fast-charging controller functioning. Additionally, the Supporting Information includes Figures S6–S7, which illustrate the overpotential contributions separated into active material and electrolyte components for the baseline cases at 25 °C across the different cell variations.

Temperature significantly affects the baseline performance. Fast-charging time (Fig. 4a) increases nearly sixfold from 45 °C to 5 °C for the Energy Cell (~33 min → ~194 min) and the Power Cell (~14 min → ~97 min). At 5 °C, the plating controller severely limits the charging current because reduced active material kinetics and electrolyte transport steepens concentration gradients and lowers the anode potential margin. The Power Cell charges roughly twice as fast as the Energy Cell at all temperatures, consistent with its shorter diffusion path.

The discharge capacity (Fig. 4b) exhibits a pronounced temperature dependence for both cell designs. For the Energy Cell, the delivered capacity decreases from approximately 4.8 Ah at 45 °C to 3.4 Ah at 25 °C, and further to only about 0.5 Ah at 5 °C, corresponding to a capacity loss of roughly 90% relative to the high-temperature case. The Power Cell shows a less pronounced temperature sensitivity, delivering approximately 3.0 Ah at 45 °C, 2.9 Ah at 25 °C, and still about 2.1 Ah at 5 °C. At 5 °C, the 1 C current creates steep concentration gradients that deplete the cathode-side electrolyte. The resulting concentration overpotential drives the cell voltage below the 2.8 V cutoff before the active material capacity is exhausted. The Energy Cell, with its longer diffusion path, reaches this transport limit earlier. This result underscores that the Energy Cell operates in a transport-limited regime at low temperatures, where even small changes in electrolyte properties can shift the usable capacity substantially. The simulated capacity loss at 5 °C is more pronounced than typically observed in commercial cells, where thermal effects and rate-adaptive protocols mitigate transport limitations. The isothermal simulation at 1 C without current adaptation represents a worst-case scenario that amplifies transport effects for the purpose of this sensitivity analysis. The investigated temperatures should therefore be interpreted as representative sensitivity states spanning the temperature range considered in this study rather than as isolated operating conditions.

The steep temperature dependence and the design-dependent transport limitations explain why parameter sensitivities amplify at low temperatures and differ between scenarios. It should be noted that the presented baseline simulations cannot be directly compared to the validation measurements of the LG M50T cell presented in [18] due to the isothermal simulation assumption. However, the parameter set and design variations provide a sufficient representation of a state-of-the-art cell for relative comparisons.

4.2. Sensitivity metric

All sensitivity results are reported as the signed relative deviation

$$\varepsilon_{\%} = \frac{X_{\mathrm{var}} - X_{\mathrm{base}}}{X_{\mathrm{base}}} \times 100\,, \tag{10}$$

where X is the output metric of the respective scenario. A positive $\varepsilon_{\%}$ indicates that the variation increases the output metric; a negative value indicates a decrease. The sign is retained in all bar charts to distinguish over- from underestimation. The heatmaps (Fig. 5a,b) display $|\varepsilon_{\%}|_{\max}$, the maximum absolute deviation per parameter and temperature.

For the fast-charging scenario, X is the charging time from 10% to 80% SoC. A closed-loop controller regulates the applied current to maintain the minimum anode potential $U_{\mathrm{plating}} \geq 10\,\mathrm{mV}$ versus $\mathrm{Li/Li^+}$, thereby preventing lithium plating. For continuous discharge, X is defined as the delivered capacity at 1,C until reaching the lower cutoff voltage of 2.8 V. These metrics provide simple indicators of cell sensitivity from the perspectives of both cell design and simulation applications. However, more complex internal cell states, such as electrolyte concentration gradients, offer deeper insights into the underlying mechanisms and are therefore partially provided in the Supporting Information (e.g., Figures S2–S5).

4.3. Fast-charging

Fig. 5 summarises $|\varepsilon_{\%}|_{\max}$ per parameter and temperature for both electrolyte variation types based on the Energy Cell results. A detailed, mechanistic analysis is given in the following sections for each scenario.

Fig. 5c,d rank all variations by $|\varepsilon_{\%}|$ at 25 °C. The five most impactful magnitude variations are: D_{app} Flat−20% (+25.9%), χ Flat+20% (+20.5%), D_{app} −20% (+11.7%), t_+^0 Flat−20% (+11.4%), and χ flat (+11.0%). Two of the top five entries involve D_{app} and two involve χ, underscoring that diffusivity and thermodynamic factor dominate the magnitude ranking during fast-charging. The shape analysis (Fig. 5d) reveals a different hierarchy, where t_+^0 can exceed both.

4.3.1. Magnitude variations and constant profiles on energy cell

Fig. 6 shows the detailed bar charts for the magnitude variations at 5, 25, and 45 °C. The apparent diffusion coefficient D_{app} dominates the magnitude sensitivity at all three temperatures. At 25 °C, the Flat−20% profile produces the largest deviation: $\varepsilon_{\%} = +25.9\%$. Uniform −20% scaling yields +11.7%, while +20% yields −7.9%. The asymmetry between +20% and −20% responses reflects the nonlinear relationship between transport parameters and concentration overpotential: reducing D_{app} steepens gradients more than an equivalent increase flattens them, because the plating controller operates closer to the transport limit in the reduction direction. A lower D_{app} steepens concentration gradients, which increases the concentration overpotential and forces the plating controller to reduce the charging current. The flat D_{app} profile at the original anchor value produces $\varepsilon_{\%} = +10.5\%$, showing that the concentration dependence of D_{app} itself contributes significantly (the mechanistic origin is detailed in Section 4.3.2).

The thermodynamic factor χ ranks second. At 25 °C, Flat+20% produces $\varepsilon_{\%} = +20.5\%$, while uniform +20% and −20% yield +8.3% and −7.9%. The mechanism operates through $\nabla \Phi_{l,\mathrm{conc}} \propto \chi \nabla \ln c$: a higher χ amplifies the concentration overpotential. The large deviation of flat profiles (+10.5% to +20.5%) versus uniform scaling (±8%) indicates that the *concentration dependence* of χ is essential.

The transference number t_+^0 shows a clear temperature trend. At 5 °C, the maximum deviation is 7.0%; at 45 °C, Flat−20% reaches 19.0%. A higher t_+^0 reduces $(1 - t_+^0)$ and suppresses the concentration gradient ($\nabla c \propto I/(F\,D_{\mathrm{app}})(1 - t_+^0)$), providing additional potential reserve.

Ionic conductivity σ is the least sensitive parameter ($|\varepsilon_{\%}| \leq 8.2\%$). Flat-profile variations are not included because a concentration-independent conductivity produces model instabilities at extreme concentrations. A constant σ removes the natural self-limiting mechanism: when local concentrations approach zero (cathode depletion), the baseline $\sigma(c)$ decreases towards zero, effectively limiting the local current density. A constant σ permits unrealistically high current densities at depleted concentrations, producing numerical divergence. This instability itself confirms that the concentration dependence of σ acts as a physical stabiliser in the model. A lower σ increases the ohmic overpotential, but the plating controller compensates by reducing the current, creating a negative feedback loop. This conclusion reflects the isolated OAT study design: the sensitivity of σ as a model parameter must be distinguished from the effect of changing the underlying physical conductivity, which is coupled with variations in viscosity and other transport functions.

4.3.2. Shape variation on energy cell

Fig. 7 shows the shape-variation sensitivity at three temperatures; the shape-sensitivity overview in Fig. 5b,d provides the corresponding heatmap and tornado ranking. The decoupling from magnitude effects reveals a qualitatively different ranking than the magnitude analysis.

Ionic conductivity σ is insensitive to shape variations during fast-charging. All non-AEM variants produce $|\varepsilon_{\%}| < 0.4\%$ at 25 °C; only the AEM curve reaches approximately 0.9%. The insensitivity reflects the controller-limited concentration range: during fast-charging, electrolyte concentrations remain close to c_{anchor}, where all shape variants coincide by construction. During discharge, cathode-side depletion drives concentrations below $0.5\,\mathrm{mol\,L^{-1}}$, where the functional form of $\sigma(c)$ at low concentrations becomes rate-determining (see Section 4.4).

The apparent diffusion coefficient D_{app} displays significant shape sensitivity. At 5 °C, the AEM-scaled profile causes $\varepsilon_{\%} = +11.7\%$, while quartering the steepness ($k \times 0.25$) yields +7.7%. Doubling the steepness ($k \times 2.0$) produces −10.3%. At 45 °C, the AEM deviation is +14.1% and the steepest profile gives −9.1%. The largest D_{app} deviations in Fig. 5b stem from the AEM-scaled profile. Without it, the maxima are 10.3%, 10.8% and 9.1% at 5 °C, 25 °C and 45 °C. The steepness parameter k governs how rapidly D_{app} decreases at concentrations above c_{anchor} and increases below c_{anchor}. During fast-charging, the anode potential acts as the rate-limiting factor, while the electrolyte salt concentration becomes depleted within the anode. As a result, D_{app} profiles that exhibit high values at low concentrations enable the shortest charging times. The strong influence of the exponential steepness parameter k suggests that measuring D_{app} across multiple concentrations — particularly at low concentrations — can substantially reduce modelling uncertainty in fast-charging applications.

The thermodynamic factor χ is moderately shape-sensitive. The wide-bathtub variant produces the largest deviation: −10.0% at 5 °C and −13.1% at 25 °C. Tail variants produce approximately 6%, indicating that the bathtub *width* is more critical than the tail type. A wider bathtub lowers χ over a broader concentration range below c_{anchor}, reducing the thermodynamic driving force for concentration equilibration.

The transference number t_+^0 exhibits the strongest temperature dependence in the shape analysis. At 5 °C, all five t_+^0-shape variants produce comparable deviations of 3%–6%. At 25 °C, Mode B fast ($c_{\mathrm{mid}} = 1.3\,\mathrm{mol\,L^{-1}}$) produces $\varepsilon_{\%} = -21.1\%$, far exceeding all other shape variations. At 45 °C, the same variant reaches $\varepsilon_{\%} = -34.8\%$ — the single largest deviation in the fast-charging analysis. During fast-charging, the anode-side electrolyte depletes while the separator side accumulates. In the DFN transport equation, the factor $(1 - t_+^0)$ determines what fraction of the reaction current produces concentration gradients. The $t_+^0(c)$ values in the depletion regime therefore directly control the gradient magnitude and the resulting concentration overpotential. All shape variants are calibrated to match the baseline at c_{anchor}. Because the Mode B fast sigmoid transitions at $c_{\mathrm{mid}} = 1.3\,\mathrm{mol\,L^{-1}}$, just above c_{anchor}, the calibration forces t_{high} above the baseline anchor value to compensate the partially active transition. As a result, Mode B fast

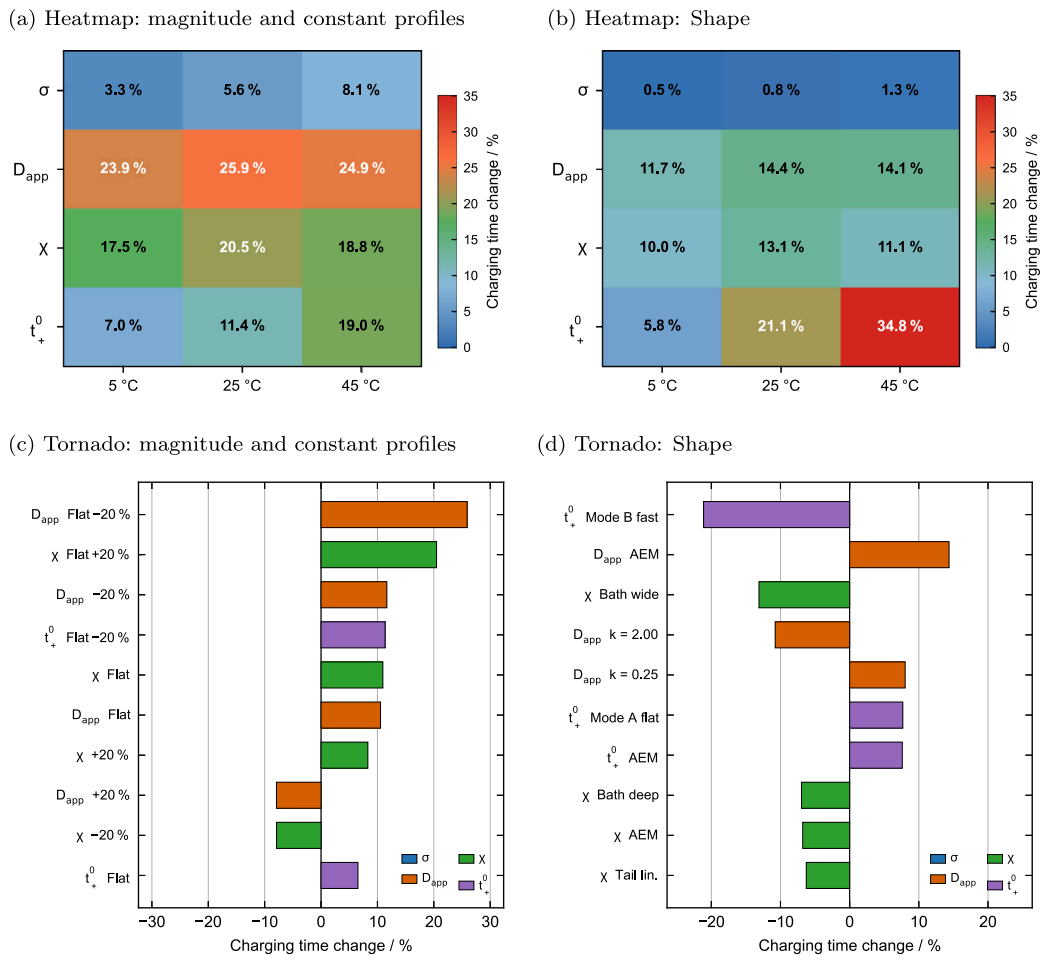


Fig. 5. Sensitivity overview for the Energy Cell, fast-charging scenario (10%–80% SoC, anode-potential control). (a, b) Maximum absolute sensitivity $|\varepsilon_{\%}|_{\max}$ per transport function (rows) and temperature (columns); colour scale from blue (<5%) to red (>20%). (c, d) Tornado ranking of all variations by $|\varepsilon_{\%}|$ at 25 °C; bars extend from zero to the signed deviation. Left column: magnitude variations and constant profiles. Right column: shape variations. (For interpretation of the references to colour in this figure legend, the reader is referred to the web version of this article.)

exhibits systematically higher t_+^0 in the depletion regime ($c < c_{\text{anchor}}$) than the baseline, reducing $(1 - t_+^0)$ and thus weakening the concentration gradient source. The weaker gradient lowers the concentration overpotential, allowing the plating controller to admit higher currents and shortening the charging time. Mode B slow ($c_{\text{mid}} = 2.0\,\text{mol}\,\text{L}^{-1}$) transitions far above the operating range, so its $t_+^0(c)$ barely differs from baseline in the depletion regime and produces only +1.8% at 25 °C. At 45 °C, higher charging currents push concentrations further from c_{anchor}, amplifying the shape differences between variants. At 5 °C, the plating controller limits the current so strongly that concentrations remain close to c_{anchor}, and all variants converge to 3%–6%. Experimentalists measuring t_+^0 at only one or two concentrations near c_{anchor} would miss the shape behaviour in the depletion regime entirely.

Although the exact magnitude of sensitivity changes varies with temperature, both variation types (magnitude and shape) yield consistent results for all parameters except partly the transference number t_+^0. Hence, the simplification of assuming isothermal conditions does not significantly affect the interpretation of parameter sensitivities.

4.3.3. Comparison of energy and power cell

Fig. 8 compares the magnitude and Fig. 9 the shape sensitivity between the Energy Cell and the Power Cell at 25 °C. The sensitivity ranking is preserved across both cell designs: D_{app} dominates, followed by χ and t_+^0 (which alternate depending on variation type), while σ is negligible.

The Energy Cell shows consistently slightly larger deviations than the Power Cell for all parameters and variation types. For t_+^0 Mode B fast (shape), the Energy Cell yields $\varepsilon_{\%} = -21.1\%$ versus −17.5% for the Power Cell. For D_{app} Flat−20% (magnitude), the values are +25.9% and +21.7%, respectively. The Energy Cell exceeds the Power Cell by a consistent factor of 1.16–1.20 in relative sensitivity. The thicker electrodes of the Energy Cell increase the electrolyte path length and thus the distance over which concentration gradients develop. At a given C-rate, the longer diffusion path produces steeper gradients and higher local concentration extremes, amplifying the sensitivity to transport parameter variations.

Despite the smaller absolute deviations, the Power Cell retains substantial electrolyte sensitivity. The t_+^0 Mode B fast variation still causes a −17.5% charging-time shift, and the D_{app} AEM profile yields +11.3%. Both values exceed 11% and are relevant for cell design decisions. The similarity arises because the plating controller adjusts the charging current in both cell designs to maintain the same 10 mV anode potential limit. In the Power Cell, the higher C-rate (resulting from thinner electrodes at the same areal current) compensates for the shorter diffusion path: the concentration gradients develop faster and reach comparable magnitudes within the shorter electrode (see Figures S2 and S3). Consequently, both cell designs operate near their respective transport limits, and the electrolyte sensitivity ranking is preserved. This controller-mediated convergence does not apply to the constant-current discharge scenario, where the fixed C-rate and shorter path length of the Power Cell genuinely reduce the gradient magnitude.

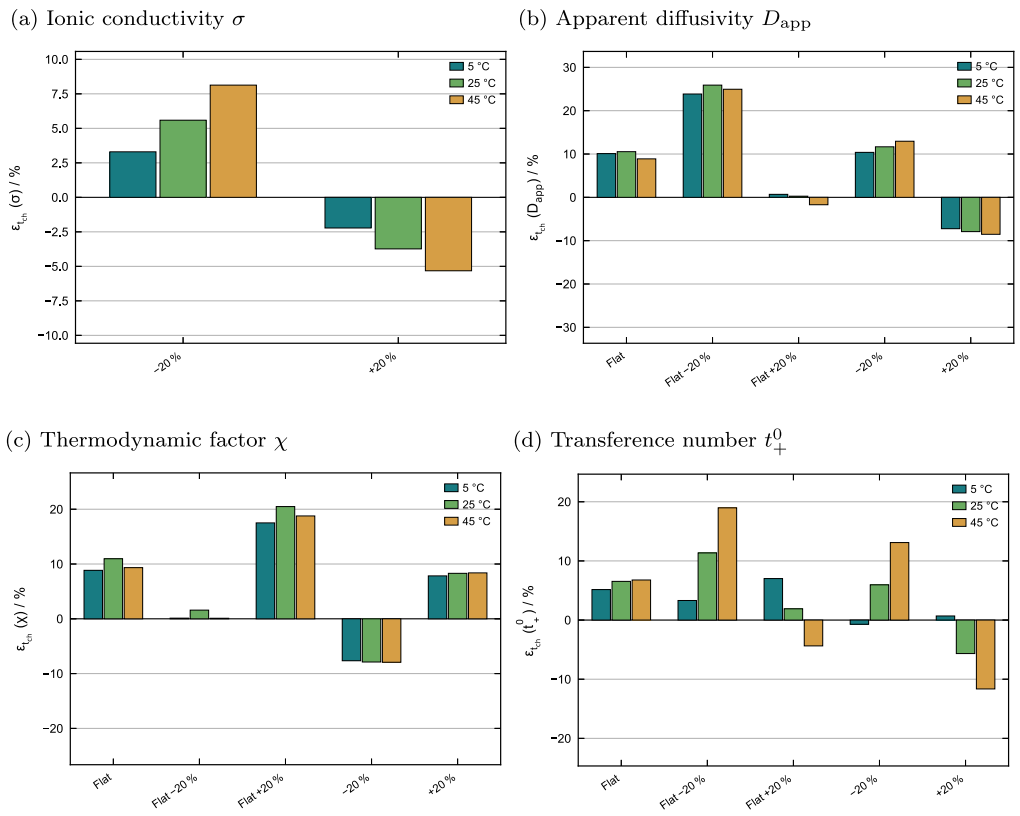


Fig. 6. Sensitivity $\varepsilon_{\%}$ to magnitude variations and constant profiles of the four electrolyte transport functions at 5 °C (blue), 25 °C (green), and 45 °C (orange). (a) Ionic conductivity σ, (b) apparent diffusivity D_{app}, (c) thermodynamic factor χ, (d) transference number t_+^0. Energy Cell, fast-charging scenario (10%–80% SoC, anode-potential control). Positive values indicate longer charging time; negative values indicate shorter. Each bar shows the deviation relative to the unperturbed baseline. (For interpretation of the references to colour in this figure legend, the reader is referred to the web version of this article.)

4.4. Continuous discharge

Since the mechanistic interpretation of transport sensitivities follows directly from Section 4.3, this section focuses on the three scenario-specific findings that distinguish discharge from fast-charging behaviour.

The discharge simulations use a lower cutoff voltage of 2.8 V and a constant-current rate of 1 C for both cell designs. Unlike fast-charging, no controller adapts the current. The cell must sustain the full applied current, which forces large concentration gradients to develop, particularly at low temperatures. As the cathode electrolyte depletes and the anode electrolyte accumulates, transport functions are evaluated at concentrations far from c_{anchor}. Detailed bar charts for all discharge variations are provided in the Supporting Information (Figs. S8–S11).

In direct comparison with the fast-charging operation, the sensitivity ranking at 25 °C and 45 °C is preserved ($D_{app} > t_+^0 > \chi > \sigma$), but absolute deviations and their temperature dependence differ substantially. In case of the Energy Cell, at 5 °C, D_{app} and χ dominate equally (each ≈71%), followed by t_+^0 (18%) and σ (7%), and discharge deviations exceed the fast-charging values for all four parameters. For example, D_{app} −20% causes $\varepsilon_{\%} = -31.9\%$ (vs. +25.9% for the largest fast-charging deviation). This amplification arises because the constant-current protocol provides no current adaptation: the fixed 1C rate drives the cell voltage below the cutoff sooner when transport limitations increase. At 25 °C and 45 °C, discharge deviations are generally smaller than in fast-charging, because the 1C rate imposes less transport stress than the plating-limited protocol.

Three scenario-specific findings emerge:

1. σ **shape becomes relevant.** During fast-charging, all σ-shape variants produce $|\varepsilon_{\%}| < 1.3\%$. During discharge at 25 °C, most σ-shape variants reach $\varepsilon_{\%} \approx -11.9\%$. The fixed 1$\dot{C}$ rate forces concentration depletion in the cathode, where the functional form of $\sigma(c)$ at low concentrations becomes relevant. The different sensitivity during fast-charging and discharge results from the different electrolyte concentration gradients, as shown in Figures S3 and S4 of the Supporting Information. During fast-charging, the electrolyte reaches less extreme concentrations, whose low conductivities would cause substantial overpotentials.
2. t_+^0 **Mode B ranking reverses.** At 25 °C discharge, Mode B slow ($c_{mid} = 2.0\,\mathrm{mol\,L^{-1}}$, $\varepsilon_{\%} = -13.9\%$) exceeds Mode B fast ($c_{mid} = 1.3\,\mathrm{mol\,L^{-1}}$, −10.7%). During fast-charging, the opposite order holds (−21.1% vs. +1.8%). The reversal reflects the different concentration ranges traversed in each scenario. During discharge, salt accumulates at the anode side into the range where Mode B slow's sigmoid transition produces $(1 - t_+^0) > 1$ (zero-crossing of t_+^0). During fast-charging, accumulation remains below the Mode B slow transition, so only Mode B fast is activated. Mode B fast's sigmoid transition near c_{anchor} raises t_{high} through the anchor calibration, elevating t_+^0 across the depletion regime and reducing $(1 - t_+^0)$.
3. D_{app} **steepness remains dominant.** Doubling k produces $\varepsilon_{\%} = -15.1\%$ at 25 °C and −15.4% at 45 °C. The Flat−20% profile yields a higher discharge capacity than baseline at 45 °C, because its elevated diffusivity at high concentrations reduces overpotential in the anode.

As in the fast-charging case, the Energy Cell exhibits significantly larger deviations than the Power Cell, and the sensitivity ranking is preserved across both cell designs. In contrast, the deviations are significantly greater during discharge due to the constant C-rate applied to both cell designs. As shown in Supporting Information Figures S4(e) and S5(e), respectively, the comparison of the maximum concentration gradient profiles at a 1 C discharge rate reveals that the Energy Cell

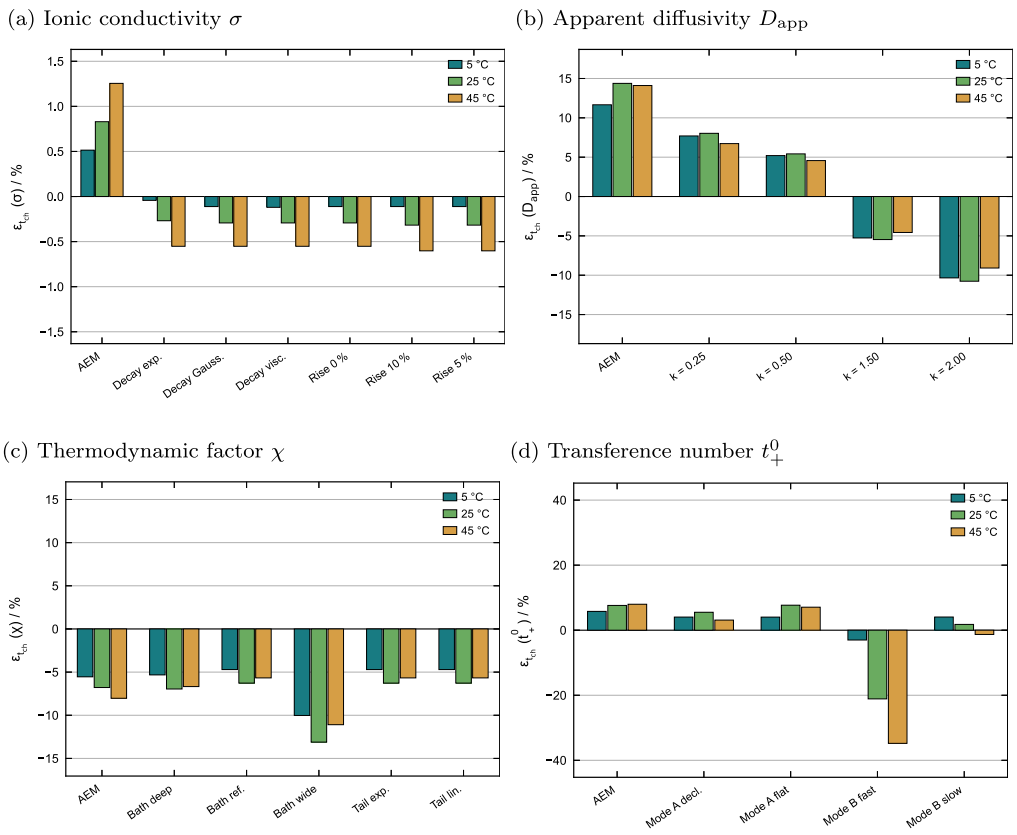


Fig. 7. Shape sensitivity $\varepsilon_{\%}$ of the four electrolyte transport functions at 5 °C (blue), 25 °C (green), and 45 °C (orange). (a) Ionic conductivity σ, (b) apparent diffusivity D_{app}, (c) thermodynamic factor χ, (d) transference number t_+^0. Energy Cell, fast-charging scenario (10%–80% SoC, anode-potential control). All shape variants preserve the baseline value at $c_{anchor} = 1.2\,mol\,L^{-1}$. Positive values indicate longer charging time; negative values indicate shorter. (For interpretation of the references to colour in this figure legend, the reader is referred to the web version of this article.)

reaches complete depletion in the positive electrode, with concentrations exceeding the specified parameter limit of $4000\,mol\,m^{-3}$. In contrast, the Power Cell maintains lithium concentrations within a stable range between 600 and $2800\,mol\,m^{-3}$. Consequently, the sensitivities determined under discharge conditions depend strongly on the cell design and the associated overpotential ratios.

4.5. Consequences for experimentalists and simulation engineers

4.5.1. Interpretation

Concentration dependence as the dominant source of uncertainty. A direct quantitative comparison between magnitude and shape sensitivities requires caution. Magnitude variations apply a uniform ±20% shift across all concentrations, whereas shape variations preserve the anchor value but may deviate by a factor of 5 or more at extreme concentrations. The comparison demonstrates that realistic variations in the functional form, as observed between independent literature sources, produce larger prediction errors than a moderate global offset. The numerical comparison applies to the variation space constructed in this study, which follows the spread between published data sets. It does not imply that shapes are inherently more impactful per percent of local change.

For three of the four transport functions at 25 °C fast-charging, removing the concentration dependence entirely (flat profiles) produces larger prediction errors than a ±20% systematic magnitude offset: D_{app} flat−20% reaches $\varepsilon_{\%} = +25.9\%$ (vs. +11.7% for D_{app} −20%), χ flat+20% reaches +20.5% (vs. +8.3% for χ +20%), and t_+^0 flat−20% reaches +11.4% (vs. +6.0% for t_+^0 −20%). Assuming concentration-independent transport functions introduces systematic errors comparable to or exceeding a 20% magnitude bias, as also qualitatively predicted in [47]. Measuring a transport property at a single concentration is therefore insufficient; instead, its concentration dependence must be characterised or may be estimated in a manner consistent with the underlying physical principles.

The shape-variation analysis identifies specific concentration -dependent features responsible for the largest prediction errors:

- D_{app}: the exponential steepness k (Eq. (7)) is the most impactful shape feature. Doubling k produces $\varepsilon_{\%} = -10.8\%$ during fast-charging and −15.1% during discharge, both at 25 °C.
- t_+^0: Mode B fast, whose anchor calibration elevates t_+^0 throughout the depletion regime, reduces $(1 - t_+^0)$ and weakens gradient buildup, producing up to $\varepsilon_{\%} = -34.8\%$ at 45 °C fast-charging. The decisive factor is the $t_+^0(c)$ profile in the depletion regime, not merely the value at c_{anchor}.
- σ: shape is irrelevant during fast-charging ($|\varepsilon_{\%}| < 1.3\%$) within the chosen variations, but reaches −11.9% during discharge at 25 °C, where concentrations depart far from c_{anchor}.
- χ: the bathtub width is more critical than the tail type. The most impactful bathtub variant produces −13.1% at 25 °C fast-charging, whereas tail variations remain below 7%.

Critical concentration regimes. During fast-charging, the plating controller constrains concentrations closer to c_{anchor} than at constant-current discharge, so measurements near and below c_{anchor} (anode depletion regime) are most relevant. The critical exception is t_+^0 with Mode B shape: the anchor calibration elevates t_+^0 throughout the depletion regime, reducing $(1 - t_+^0)$ and weakening gradient buildup. This allows the plating controller to admit higher currents, producing the largest single deviation in the fast-charging analysis (−34.8% at 45 °C). During constant-current discharge, cathode-side depletion below $0.8\,mol\,L^{-1}$ degrades all four transport functions simultaneously — a compound effect not captured by the present one-at-a-time analysis. Discharge-oriented measurement campaigns with application close to

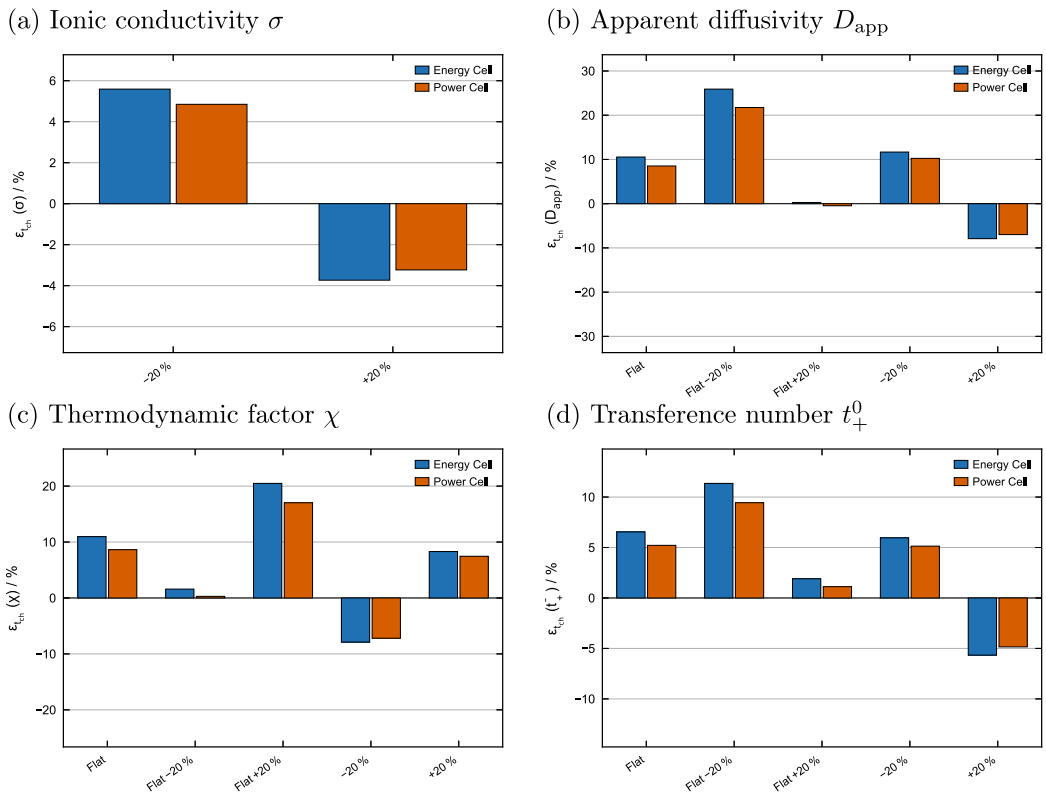


Fig. 8. Sensitivity $\varepsilon_{\%}$ comparison for magnitude variations and constant profiles between Energy Cell (filled bars) and Power Cell (hatched bars) at 25 °C, fast-charging scenario (10%–80% SoC, anode-potential control). (a) σ, (b) D_{app}, (c) χ, (d) t_+^0. Each bar shows $\varepsilon_{\%}$ relative to the respective cell's baseline.

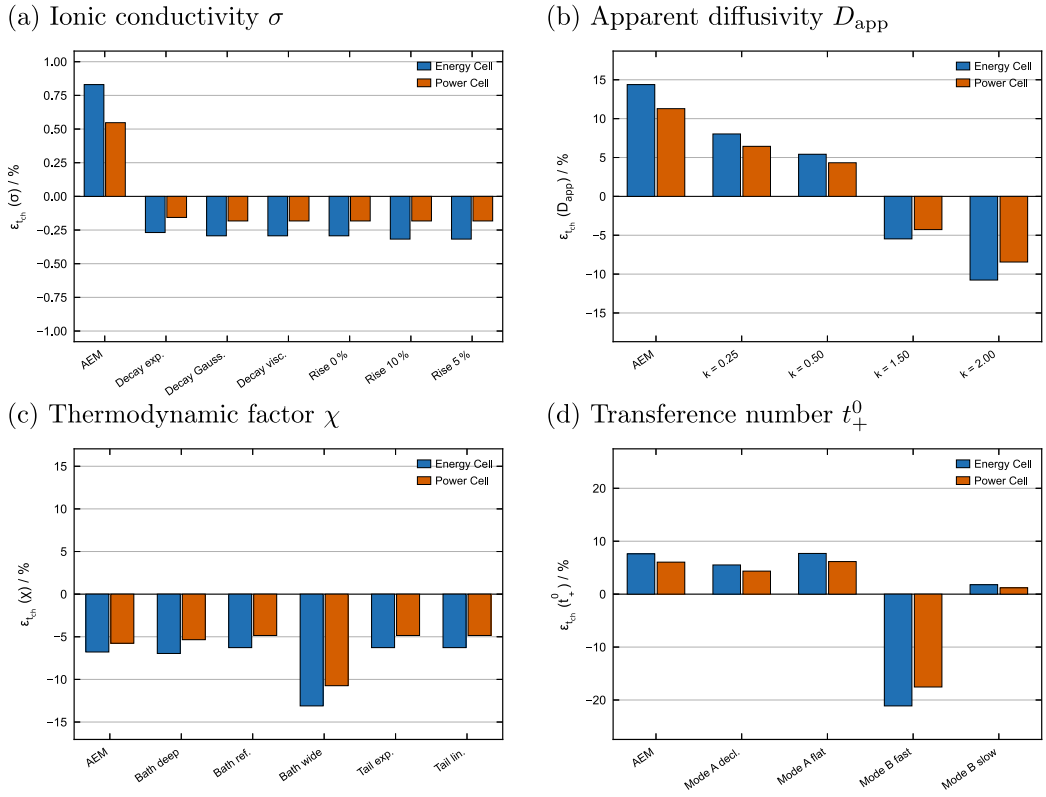


Fig. 9. Shape sensitivity $\varepsilon_{\%}$ comparison between Energy Cell (filled bars) and Power Cell (hatched bars) at 25 °C, fast-charging scenario (10%–80% SoC, anode-potential control). (a) σ, (b) D_{app}, (c) χ, (d) t_+^0. All shape variants preserve the baseline value at c_{anchor}. Each bar shows $\varepsilon_{\%}$ relative to the respective cell's baseline.

the cell's power limits should therefore prioritise the range 0.3–0.8 mol L^{-1}. Dedicated experimental methods for these concentration ranges are under development in our group. A first step reduces the number of measurements required to resolve $\sigma(c,T)$ [45]. Corresponding protocols for D_{app} and t_+^0, covering the depletion regime and the high-concentration behaviour of t_+^0, will be reported separately.

System and scenario dependence. Three factors control the severity of electrolyte sensitivity. *Cell design:* Thicker electrodes (Energy Cell) produce larger deviations, but the Power Cell remains sensitive during fast-charging due to the plating controller. *Temperature:* Towards 5 °C, discharge sensitivity amplifies nonlinearly (for example, D_{app} ±20% scaling: 4.0-fold from 45 °C to 5 °C). Fast-charging magnitude sensitivity shows only moderate temperature dependence. Cold-climate applications impose the most demanding requirements. Temperatures below 5 °C were not simulated. Effects such as salt precipitation, solvent crystallisation and lithium plating are not described by the model. *Operating mode:* Fast-charging defines the accuracy ceiling, e.g. in automotive applications, operating continuously near the transport limit. Drive-cycle sensitivity is expected to be lower, though transient high-rate pulses were not investigated. *Active material:* Cells with slower solid-state kinetics shift the voltage budget towards electrode overpotentials, reducing the relative weight of electrolyte transport [14,20]. Consequently, the quantitative electrolyte sensitivities reported here may differ for electrode materials with substantially different rate capabilities.

Sensitivity-based prioritisation. The sensitivity hierarchy depends on operating scenario and temperature (Figs. 5 and 6). A single sensitivity ranking does not exist. The transference number t_+^0 is an instructive case: its ±20% scaling sensitivity is negligible at 5 °C fast-charging ($|\varepsilon_{\%}| \leq 0.8\%$) but rises sharply with temperature, reaching 13.1% at 45 °C during fast-charging. Conversely, σ is nearly insensitive at 45 °C discharge (< 1.3%) but reaches moderate relevance at 5 °C discharge (7.2%), where reduced ionic mobility in the electrolyte begins to matter. Experimentalists must consider the target operating conditions before setting measurement priorities.

Quantitative accuracy thresholds. The following paragraphs translate the sensitivity results into quantitative accuracy requirements and practical recommendations.

For a model application in battery cell design, we assume a target KPI tolerance of $|\varepsilon_{\%}| \leq 10\%$ for the predicted fast-charging time and $|\varepsilon_{\%}| \leq 5\%$ for the discharge capacity at 1 C. These relatively tight target tolerances arise from the need to include design margins, which may otherwise introduce conflicting design constraints or increase costs. Table 3 converts the ±20% scaling results into maximum allowable parameter errors for these prediction tolerances, assuming that the concentration dependence is captured correctly. This simplification is necessary due to the virtually unlimited number of possible variations in concentration dependence. The derivation assumes local linearity: a sensitivity gain $g = |\varepsilon_{\%}|/20$ converts the perturbation into a proportionality factor, and the required accuracy follows as $\Delta_{max} = |\varepsilon_{\%}|/g_{max}$, where g_{max} is the larger of the two gains (from +20% and −20%). The resulting thresholds are approximate estimates intended to guide measurement prioritisation, not exact tolerance specifications.

The apparent diffusion coefficient D_{app} imposes the strictest accuracy requirement across all operating conditions. During fast-charging, D_{app} must be determined within ±15–19%, depending on temperature. Under 5 °C discharge, this requirement tightens to ±1.4%, which is substantially below the typical inter-study variation reported in Table 1. Even a 5% error in D_{app} leads to a considerable capacity deviation under these conditions. This highlights that D_{app} must be measured with the highest accuracy and for the specific electrolyte formulation used in the target cell. However, this stringent requirement at 5 °C should be interpreted with caution. It arises from an extremely transport-limited regime, and the isothermal simulation predicts a capacity loss that is stronger than typically observed experimentally (Fig. 4b). This discrepancy is mainly caused by the isothermal assumption adopted in this study. Based on the 1 C discharge measurements of the original LG M50T 21700 cell reported in [18], self-heating to approximately 25 °C can be expected, which results in a higher retained capacity than predicted by the isothermal simulation (Fig. 4b). The very high sensitivity at 5 °C therefore represents a conservative, worst-case estimate rather than a typical requirement. Under such practically relevant conditions, the tolerance relaxes to about ±4%. Moreover, applying such a strict tolerance at the absolute electrolyte depletion limit should be treated critically, as practical cell designs would likely be modified to avoid operation near this limit. This is evident, for example, for the 1 C discharge at 45 °C. Therefore, a tolerance of approximately ±10% in D_{app} is considered a more realistic requirement for operating conditions relevant to practical cell design. For operation above 5 °C, an approximate tolerance of ±15% is sufficient for all other parameters under the assumed prediction tolerances. In contrast, fast-charging conditions are more directly transferable to accuracy requirements because they are governed by a more clearly defined operational limit.

Table 3
Maximum allowable measurement error Δ_{max} (%) of the transport parameter magnitude for a prediction tolerance of $|\varepsilon_{\%}| \leq 10\%$ for fast-charging time and $|\varepsilon_{\%}| \leq 5\%$ for discharge capacity. Values derived from linear interpolation of the ±20% scaling results (Energy Cell). Entries marked > 20 indicate that a ±20% magnitude error produces $|\varepsilon_{\%}| < 5\%$ and that magnitude accuracy at this level is not a binding constraint.

	Fast-charging			Discharge (1C)		
Parameter	5 °C	25 °C	45 °C	5 °C	25 °C	45 °C
D_{app}	±19.3	±17.1	±15.4	±1.4	±4.0	±12.5
χ	±25.5	±24.1	±23.9	±7.4[a]	±18.8	≫20
t_+^0	≫ 20[b]	±33.6	±15.3	≫ 20[b]	±16.7	±29.3
σ	≫20	±35.8	±24.6	±13.8[c]	±33.2	≫20

[a] Nearly symmetric at 5 °C discharge (+20% → +13.6%, −20% → −12.6%).
[b] ±20% magnitude scaling produces $|\varepsilon_{\%}| \leq 0.8\%$; shape effects dominate (e.g. Mode B fast: $|\varepsilon_{\%}| = 21.1\%$ at 25 °C fast-charging).
[c] Asymmetric: predominantly sensitive to underestimation (−20% → +7.2%, +20% → −4.8%).

Limitations. The following limitations apply to the present analysis and should be considered when interpreting the quantitative thresholds.

1. **Parameter interactions are only partly captured.** The OAT variations perturb D_{app}, t_+^0 and χ in isolation, but Eqs. (3) and (4) depend on them only through the groups $D_{app}/(1-t_+^0)$(concentration gradient) and $(1-t_+^0)\,\chi$(diffusion potential). A coupled study shown in the Supporting Information (Figs. S13–S15) confirms that fast-charging predictions depend on these groups, not the individual functions, to within 0.17 percentage points. Table 3 should be read accordingly, and errors within a group can cancel or add. For example, a +20% error in D_{app} at 25 °C shortens the energy cell's charge time by 7.9% if t_+^0 is independent, but lengthens it by 8.4% if t_+^0 is coupled to preserve $D_{app}/(1-t_+^0)$ – transport data should thus come from one consistent campaign. The grouping does not hold during transport-limited discharge at 5 °C, where the per-function thresholds remain necessary (difference up to 10.2 percentage points). Combined errors in both groups, in σ, or in the functions' concentration dependence were not simulated and cannot be inferred by summing single-parameter results.
2. **Only electrolyte transport functions were varied.** Previous global sensitivity analyses [17,38] showed that electrode parameters, such as solid diffusivity and exchange current density, dominate the total output variance at moderate C-rates. At high rates and low temperatures, however, electrolyte transport becomes increasingly important. The present study specifically quantifies the electrolyte contribution in the transport-limited regime.

3. **Electrolyte parameter activation energies were not varied separately.** Every simulation runs at a fixed temperature. At a fixed temperature, an error in the activation energy only scales a transport function by a constant factor, $\exp[-\Delta E_a/R(1/T - 1/T_{ref})]$. This is precisely what the ±20% magnitude variations do. Activation-energy errors are therefore already covered, and the equivalent error can be quantified. At 5 °C, referenced to 25 °C, a ±20% shift corresponds to an activation-energy error of 6.3 to 7.7 kJ mol^{-1}. The baseline values at c_{anchor} are 13.0 kJ mol^{-1} for σ and 17.8 kJ mol^{-1} for D_{app}. The variations thus span 35% to 60% of the baseline activation energy. One case remains outside this equivalence. An activation energy that itself depends on concentration changes the curve shape, and the shape variations represent that case.
4. **Sensitivity depends on electrode kinetics.** The quantitative accuracy requirements are linked to the rate capability of the electrode active materials and microstructure. Cells with substantially different active material parameters may exhibit different electrolyte sensitivities.
5. **Spatial temperature gradients and overall heating were not considered.** Real cells exhibit temperature differences between core and surface as well as transient temperature evolution during operation. The isothermal simulations at 5, 25, and 45 °C were deliberately chosen to isolate the temperature dependence of electrolyte-parameter sensitivity independently of a specific thermal-management scenario. An explicit thermal model would require additional assumptions regarding cooling conditions and thermal boundary parameters, making the resulting sensitivities more system-specific. The present approach therefore provides temperature-resolved sensitivity information over the investigated range of 5—45 °C, whereas electrothermal simulations would be required to quantify sensitivities along a specific transient temperature trajectory.
6. **Only two operating modes were investigated.** The study considered plating-limited fast-charging and 1 C discharge only. Intermediate C-rates and dynamic operating profiles are expected to yield lower sensitivities [16,38], but were not quantified. The comparison of the two cell designs behaves analogously to a rate variation, as a given C-rate produces smaller concentration gradients in thinner than in thicker electrodes. Since the analysis is intended to be general, it is not restricted to automotive driving cycles and also applies, e.g., to power tools.
7. **The findings are limited to conventional DFN models.** Effects related to microstructure, such as electrolyte-motion-induced salt inhomogeneity [48] or electrolyte penetration into polycrystalline particles as described in [49], may lead to an increased electrolyte sensitivity beyond the effects captured in conventional DFN frameworks.

4.5.2. *Recommendations for simulation engineers*

Based on the sensitivity results, the following practical guidelines are proposed for parameterising electrolyte transport functions in DFN models.

1. **Avoid concentration-independent transport functions.** Flat profiles may produce errors comparable to or exceeding ±20% magnitude bias. If measured concentration-dependent data is unavailable for the target electrolyte, adopt a physically motivated profile from a similar solvent system rather than assuming a constant value. Even an approximate functional form significantly reduces the prediction error compared to a flat profile.
2. **Match the electrolyte formulation.** Parameter sets are generally not transferable across solvent systems. The concentration dependence — the primary uncertainty source — varies qualitatively between EC:EMC, EC:DMC, and other formulations [35, 45]. Cross-solvent transfer invalidates both the shape and the magnitude of each transport function.
3. **Prioritise measurements at low concentrations.** For D_{app} and σ, the dominant sensitivity arises from the low-concentration regime ($c < c_{anchor}$). A dilution series from the reference electrolyte may therefore provide sufficient characterisation of the critical concentration range. For t_+^0, however, the sign at $c > 1.5$ mol L^{-1} is decisive and cannot be inferred from dilution experiments alone.
4. **Validate low-temperature predictions experimentally.** At 5 °C, the discharge sensitivity of all four parameters is amplified, and their effects may compound. Model predictions at 5 °C and below should be treated as qualitative unless validated against discharge data. For the highest level of accuracy, electrolyte parameter sets should be re-fitted. Otherwise, achieving such target accuracies may become unrealistic. In other words, parameter sets can be transferred between projects, but re-measurement alone will likely not provide sufficient precision. Even if experimental improvements in parameter accuracy do not fully meet the target metrics, they can significantly constrain parameter bounds for optimisation procedures and reduce uncertainty margins.
5. **For $T \geq 25$ °C and moderate C-rates,** the requirements relax substantially. σ and χ tolerate > |20|% magnitude errors, and σ shape should be close to typical literature curves.

5. Conclusion

This study introduced a dual variation strategy that decouples magnitude and concentration-dependence (shape) effects of four electrolyte transport functions on DFN battery model predictions. The sensitivity hierarchy depends on the operating scenario: during fast-charging at 25 °C, $D_{app} > \chi > t_+^0 > \sigma$; during 5 °C discharge, D_{app} and χ dominate equally, followed by t_+^0 and σ. For three of four parameters, removing the concentration dependence produces larger prediction errors than a 20% systematic magnitude bias. This comparison applies to the variation space constructed in this study.

The apparent diffusion coefficient D_{app} imposes the tightest accuracy requirement: ±17.1% for fast-charging at 25 °C and nominally ±1.4% for isothermal 5 °C discharge; under realistic conditions with self-heating, a tolerance of approximately ±10% is considered sufficient for practical cell design. The $t_+^0(c)$ profile across the operating range matters more than its value at a single concentration: a Mode B fast shape whose anchor calibration elevates t_+^0 in the depletion regime, reducing $(1 - t_+^0)$ and weakening gradient buildup, produces the single largest fast-charging deviation (−34.8% at 45 °C). Ionic conductivity σ concentration-dependence is negligible during fast-charging but reaches −11.9% during 25 °C discharge, demonstrating that the operating mode determines which curve features are relevant. Towards 5 °C, the discharge sensitivities to D_{app}, χ and σ amplify nonlinearly and tighten the corresponding thresholds in Table 3. The ranking is preserved across Energy and Power Cell designs, confirming that the results are not specific to a single electrode geometry.

These findings establish that single-concentration parameterisations are insufficient and that the concentration dependence, particularly the D_{app} steepness at low concentrations and the t_+^0 sign at $c > 1.5$ mol L^{-1}, must be experimentally resolved. Experimental protocols targeting these two concentration regimes are under development and will be reported in future work, together with a comparison of predicted and measured transport functions for further electrolyte formulations. Additionally, several practical recommendations have been developed for experimentalists and simulation engineers working with electrolyte parameters in the context of P2D modelling. The one-at-a-time design does not capture parameter interactions; multivariate perturbation studies are needed to quantify coupled effects. The accuracy thresholds are specific to the electrode kinetics studied and require re-evaluation for cells with substantially different rate capability.

CRediT authorship contribution statement

Maximilian Gruber: Writing – original draft, Visualization, Methodology, Investigation, Formal analysis, Conceptualization. **Jonas Günther:** Writing – original draft, Visualization, Methodology, Investigation, Formal analysis, Conceptualization. **Frank Hofmann:** Writing – review & editing, Supervision, Methodology. **Daniel Rutz:** Writing – review & editing, Supervision. **Dominik Wycisk:** Writing – review & editing, Conceptualization. **Nils Stumböck:** Writing – review & editing, Visualization. **Marc Oldenburger:** Writing – review & editing, Supervision. **Ernst Richter:** Writing – review & editing, Methodology. **Ralf Moos:** Writing – review & editing, Supervision. **Jan Philipp Schmidt:** Writing – review & editing, Supervision. **André Weber:** Writing – review & editing, Supervision.

Declaration of competing interest

The authors declare the following financial interests/personal relationships which may be considered as potential competing interests: Maximilian Gruber reports financial support was provided by Mercedes-Benz AG. Jonas Guenther reports financial support was provided by Mercedes-Benz AG. If there are other authors, they declare that they have no known competing financial interests or personal relationships that could have appeared to influence the work reported in this paper.

Acknowledgements

The authors acknowledge the use of an AI-based language model (ChatGPT, OpenAI and Claude, Anthropic) for language editing and stylistic refinement during manuscript preparation. All scientific content, interpretations, and conclusions were critically reviewed and remain the sole responsibility of the authors.

Appendix A. Supplementary data

Supplementary material related to this article can be found online at https://doi.org/10.1016/j.est.2026.125582.

Data availability

Data will be made available on request.

References

[1] M. Doyle, T.F. Fuller, J. Newman, Modeling of galvanostatic charge and discharge of the lithium/polymer/insertion cell, J. Electrochem. Soc. 140 (6) (1993) 1526–1533, http://dx.doi.org/10.1149/1.2221597.

[2] T.F. Fuller, M. Doyle, J. Newman, Simulation and optimization of the dual lithium ion insertion cell, J. Electrochem. Soc. 141 (1) (1994) 1–10.

[3] A.A. Wang, S.E.J. O'Kane, F. Brosa Planella, J.L. Houx, K. O'Regan, M. Zyskin, J. Edge, C.W. Monroe, S.J. Cooper, D.A. Howey, E. Kendrick, J.M. Foster, Review of parameterisation and a novel database (liiondb) for continuum li-ion battery models, Prog. Energy 4 (3) (2022) 032004, http://dx.doi.org/10.1088/2516-1083/ac692c.

[4] E.C. Tredenick, A.M. Boyce, S. Wheeler, J. Li, Y. Sun, R. Drummond, S.R. Duncan, P.S. Grant, P.R. Shearing, Bridging the gap between microstructurally resolved computed tomography-based and homogenised doyle-fuller-newman models for lithium-ion batteries, J. Electrochem. Soc. 172 (3) (2025) 030503, http://dx.doi.org/10.1149/1945-7111/adb684.

[5] J. Newman, K.E. Thomas-Alyea, Electrochemical Systems, third ed., John Wiley & Sons, Hoboken, NJ, 2004, Standard textbook covering transport phenomena, thermodynamics and kinetics in electrochemical systems; provides the theoretical basis for concentrated-solution theory in battery models..

[6] V. Sulzer, S.G. Marquis, R. Timms, M. Robinson, S.J. Chapman, Python battery mathematical modelling (PyBaMM), J. Open Source Softw. 6 (64) (2021) 3186, http://dx.doi.org/10.5334/jors.309, Introduces the open-source PyBaMM framework for flexible implementation and comparison of physics-based battery models using an expression-tree approach..

[7] K. Xu, Nonaqueous liquid electrolytes for lithium-based rechargeable batteries, Chem. Rev. 104 (10) (2004) 4303–4418, http://dx.doi.org/10.1021/cr030203g, Seminal review of non-aqueous electrolyte chemistry covering solvents, salts, additives, SEI formation and transport properties for lithium-ion batteries..

[8] Q. Liu, C. Du, B. Shen, P. Zuo, X. Cheng, Y. Ma, G. Yin, Y. Gao, Understanding undesirable anode lithium plating issues in lithium-ion batteries, "RSC Adv." 6 (2016) 88683–88700, http://dx.doi.org/10.1039/C6RA19482F.

[9] Q. Li, G. Liu, H. Cheng, Q. Sun, J. Zhang, J. Ming, Low-temperature electrolyte design for lithium-ion batteries: Prospect and challenges, Chem. – A Eur. J. 27 (64) (2021) 15842–15865, http://dx.doi.org/10.1002/chem.202101407.

[10] C. Fan, K. Zhang, Q. Peng, J. Tian, K. Liu, C.Y. Chung, Fast characterization of lithium-ion battery impedance and nonlinearity using optimized multisine perturbation signal, IEEE Trans. Ind. Electron. 72 (2025) 11395–11405, http://dx.doi.org/10.1109/TIE.2025.3561879.

[11] C.-J. Ko, K.-C. Chen, Using tens of seconds of relaxation voltage to estimate open circuit voltage and state of health of lithium ion batteries, Appl. Energy 357 (2024) 122488, http://dx.doi.org/10.1016/j.apenergy.2023.122488.

[12] X. Ke, H. Hong, P. Zheng, S. Zhang, L. Zhu, Z. Li, J. Cai, P. Fan, J. Yang, J. Wang, L. Li, C. Kuai, Y. Guo, State-of-health estimation for lithium-ion batteries using relaxation voltage under dynamic conditions, J. Energy Storage 100 (2024) 113506, http://dx.doi.org/10.1016/j.est.2024.113506.

[13] M. Ecker, T.K.D. Tran, P. Dechent, S. Käbitz, A. Warnecke, D.U. Sauer, Parameterization of a physico-chemical model of a lithium-ion battery: I. Determination of parameters, J. Electrochem. Soc. 162 (9) (2015) A1836, http://dx.doi.org/10.1149/2.0551509jes.

[14] C.-H. Chen, F. Brosa Planella, K. O'Regan, D. Gastol, W.D. Widanage, E. Kendrick, Development of experimental techniques for parameterization of multi-scale lithium-ion battery models, J. Electrochem. Soc. 167 (8) (2020) 080534, http://dx.doi.org/10.1149/1945-7111/ab9050.

[15] M. Safari, M. Morcrette, A. Teyssot, C. Delacourt, Multimodal physics-based aging model for life prediction of Li-ion batteries, J. Electrochem. Soc. 156 (3) (2009) A145–A153, http://dx.doi.org/10.1149/1.3043429.

[16] E. Zonta, I.J. Buha, M. Spinola, C. Weißinger, H.-J. Bungartz, A. Jossen, Time-dependent global sensitivity analysis of the doyle–fuller–newman model, J. Energy Storage 158 (2026) 121751, http://dx.doi.org/10.1016/j.est.2026.121751.

[17] J. Chen, S.P. Mattus, W. Cao, D.U. Sauer, W. Li, Global sensitivity analysis towards non-invasive parameterization of the electrochemical-thermal model for lithium-ion batteries, Adv. Appl. Energy 18 (2025) 100221, http://dx.doi.org/10.1016/j.adapen.2025.100221.

[18] K. O'Regan, F. Brosa Planella, W.D. Widanage, E. Kendrick, Thermal-electrochemical parameters of a high energy lithium-ion cylindrical battery, Electrochim. Acta 425 (2022) 140700, http://dx.doi.org/10.1016/j.electacta.2022.140700.

[19] S.E.J. O'Kane, W. Ai, G. Madabattula, D. Alonso-Alvarez, R. Timms, V. Sulzer, J.S. Edge, B. Wu, G.J. Offer, M. Marinescu, Lithium-ion battery degradation: how to model it, "Phys. Chem. Chem. Phys." 24 (2022) 7909–7922, http://dx.doi.org/10.1039/D2CP00417H.

[20] R. Li, N.D. Kirkaldy, F.F. Oehler, et al., The importance of degradation mode analysis in parameterising lifetime prediction models of lithium-ion battery degradation, Nat. Commun. 16 (2025) 2776, http://dx.doi.org/10.1038/s41467-025-57968-3.

[21] J. Landesfeind, H.A. Gasteiger, Temperature and concentration dependence of the ionic transport properties of lithium-ion battery electrolytes, J. Electrochem. Soc. 166 (14) (2019) A3079, http://dx.doi.org/10.1149/2.0571912jes.

[22] A. Nyman, M. arten Behm, G. Lindbergh, Electrochemical characterisation and modelling of the mass transport phenomena in LiPF6–EC–EMC electrolyte, Electrochim. Acta 53 (22) (2008) 6356–6365, http://dx.doi.org/10.1016/j.electacta.2008.04.023.

[23] A.A. Wang, T. Hou, M. Karanjavala, C.W. Monroe, Shifting-reference concentration cells to refine composition-dependent transport characterization of binary lithium-ion electrolytes, Electrochim. Acta 358 (2020) 136688, http://dx.doi.org/10.1016/j.electacta.2020.136688.

[24] J. Landesfeind, T. Hosaka, M. Graf, K. Kubota, S. Komaba, H.A. Gasteiger, Comparison of ionic transport properties of non-aqueous lithium and sodium hexafluorophosphate electrolytes, J. Electrochem. Soc. 168 (4) (2021) 040538, http://dx.doi.org/10.1149/1945-7111/abf8d9.

[25] H. Lundgren, Thermal Aspects and Electrolyte Mass Transport in Lithium-ion Batteries (Ph.D. thesis), in: TRITA-CHE-Report, (2015:22) KTH, Applied Electrochemistry, 2015, p. 60, QC 20150522.

[26] A. Ehrl, J. Landesfeind, W.A. Wall, H.A. Gasteiger, Determination of transport parameters in liquid binary lithium ion battery electrolytes, J. Electrochem. Soc. 164 (4) (2017) A826, http://dx.doi.org/10.1149/2.1131704jes.

[27] L. Lehnert, M. Nojabaee, A. Latz, B. Horstmann, Challenges in measuring transport parameters of carbonate-based electrolytes, ChemElectroChem 11 (11) (2024) e202400056, http://dx.doi.org/10.1002/celc.202400056.

[28] L. Lehnert, M. Lorenz, M.F. Juarez, M. Schammer, M. Nojabaee, M. Schönhoff, B. Horstmann, Combining molecular dynamics and experimental methods for the parametrization of binary carbonate-based electrolytes, J. Electrochem. Soc. 172 (5) (2025) 050523, http://dx.doi.org/10.1149/1945-7111/add381.

[29] L.O. Valøen, J.N. Reimers, Transport properties of LiPF6-based li-ion battery electrolytes, J. Electrochem. Soc. 152 (5) (2005) A882, http://dx.doi.org/10.1149/1.1872737.

[30] D.T. Hickson, D.M. Halat, A.S. Ho, J.A. Reimer, N.P. Balsara, Complete characterization of a lithium battery electrolyte using a combination of electrophoretic NMR and electrochemical methods, "Phys. Chem. Chem. Phys." 24 (2022) 26591–26599, http://dx.doi.org/10.1039/D2CP02622H.

[31] D.M. Pesko, K. Timachova, R. Bhattacharya, M.C. Smith, I. Villaluenga, J. Newman, N.P. Balsara, Negative transference numbers in poly(ethylene oxide)-based electrolytes, J. Electrochem. Soc. 164 (11) (2017) E3569, http://dx.doi.org/10.1149/2.0581711jes.

[32] Y. Shao, H. Gudla, D. Brandell, C. Zhang, Transference number in polymer electrolytes: Mind the reference-frame gap, J. Am. Chem. Soc. 144 (17) (2022) 7583–7587, http://dx.doi.org/10.1021/jacs.2c02389, PMID: 35446043.

[33] K.D. Fong, J. Self, K.M. Diederichsen, B.M. Wood, B.D. McCloskey, K.A. Persson, Ion transport and the true transference number in nonaqueous polyelectrolyte solutions for lithium ion batteries, ACS Central Sci. 5 (7) (2019) 1250–1260, http://dx.doi.org/10.1021/acscentsci.9b00406, PMID: 31403073.

[34] S. Stewart, J. Newman, Measuring the salt activity coefficient in lithium-battery electrolytes, J. Electrochem. Soc. 155 (6) (2008) A458, http://dx.doi.org/10.1149/1.2904526.

[35] K.L. Gering, Prediction of electrolyte viscosity for aqueous and non-aqueous systems: Results from a molecular model based on ion solvation and a chemical physics framework, Electrochim. Acta 51 (15) (2006) 3125–3138, http://dx.doi.org/10.1016/j.electacta.2005.09.011.

[36] Ridgetop Group, K.L. Gering, Advanced electrolyte model (AEM) software, 2024, Commercial software implementing the AEM framework for predicting all four transport functions simultaneously for arbitrary salt–solvent combinations..

[37] E.R. Logan, E.M. Tonita, K.L. Gering, J.R. Dahn, A critical evaluation of the advanced electrolyte model, J. Electrochem. Soc. 165 (14) (2018) A3350, http://dx.doi.org/10.1149/2.0471814jes.

[38] M. Hadigol, K. Maute, A. Doostan, On uncertainty quantification of lithium-ion batteries: Application to an LiC6/LiCoO2 cell, J. Power Sources 300 (2015) 507–524, http://dx.doi.org/10.1016/j.jpowsour.2015.09.060.

[39] W. Li, D. Cao, D. Jöst, F. Ringbeck, M. Kuipers, F. Frie, D.U. Sauer, Parameter sensitivity analysis of electrochemical model-based battery management systems for lithium-ion batteries, Appl. Energy 269 (2020) 115104, http://dx.doi.org/10.1016/j.apenergy.2020.115104.

[40] S. Ma, B. Sun, X. Su, W. Zhang, H. Ruan, Sensitivity analysis of electrochemical model parameters for lithium-ion batteries on terminal voltages and anode lithium plating criterion, J. Energy Storage 71 (2023) 108127, http://dx.doi.org/10.1016/j.est.2023.108127.

[41] A.S. Keefe, S. Buteau, I.G. Hill, J.R. Dahn, Temperature dependent EIS studies separating charge transfer impedance from contact impedance in lithium-ion symmetric cells, J. Electrochem. Soc. 166 (14) (2019) A3272–A3279, http://dx.doi.org/10.1149/2.0541914jes.

[42] J. Günther, D. Wycisk, R. Siva Dev, A. Fill, K.P. Birke, R. Moos, J.P. Schmidt, M. Oldenburger, Determination of the solid state diffusion coefficient of Li-ion battery single-phase materials using thin model electrodes, J. Electrochem. Soc. 172 (3) (2025) 030525, http://dx.doi.org/10.1149/1945-7111/adbfc5.

[43] F. Kohlrausch, L. Holborn, Das leitvermögen der elektrolyte, insbesondere der lösungen, methoden, resultate und chemische anwendungen., Z. Elektrochem. 5 (21) (1898) 248, http://dx.doi.org/10.1002/bbpc.18980052106.

[44] P. de Blasio, J. Elsborg, T. Vegge, E. Flores, A. Bhowmik, CALiSol-23: Experimental electrolyte conductivity data for various Li-salts and solvent combinations, "Scientific Data" 11 (1) (2024) 750.

[45] M. Gruber, D. Rutz, F. Hofmann, A. Weber, Minimizing experimental effort: A two-equation model for wide-range ionic conductivity in lithium-ion battery electrolytes, J. Electrochem. Soc. 173 (12) (2026) 120518, http://dx.doi.org/10.1149/1945-7111/ae7d5b.

[46] J. Self, K.D. Fong, K.A. Persson, Transport in superconcentrated LiPF6 and LiBF4/Propylene carbonate electrolytes, ACS Energy Lett. 4 (12) (2019) 2843–2849, http://dx.doi.org/10.1021/acsenergylett.9b02118.

[47] P. Hashemzadeh, M. Désilets, M. Lacroix, A. Jokar, Investigation of the P2D and of the modified single-particle models for predicting the nonlinear behavior of li-ion batteries, J. Energy Storage 52 (2022) 104909, http://dx.doi.org/10.1016/j.est.2022.104909.

[48] S. Solchenbach, C. Tacconis, A. Gomez Martin, V. Peters, L. Wallisch, A. Stanke, J. Hofer, D. Renz, B. Lewerich, G. Bauer, M. Wichmann, D. Goldbach, A. Adam, M. Spielbauer, P. Lamp, J. Wandt, Electrolyte motion induced salt inhomogeneity – a novel aging mechanism in large-format lithium-ion cells, "Energy Env. Sci." 17 (2024) 7294–7317, http://dx.doi.org/10.1039/D4EE03211J.

[49] J. Günther, J. Lim, M. Ronowski, D. Wycisk, M. Oldenburger, T. Glossmann, Y. Li, R. Moos, J.P. Schmidt, Impact of particle size on kinetics and transport in polycrystalline Li-ion battery materials: Comparing thin-electrode and single-particle measurements, J. Electrochem. Soc. 173 (10) (2026) 100514, http://dx.doi.org/10.1149/1945-7111/ae6e9a.